# MODEL OF TWO-PHASE MOTOR AND COMPRESSOR FOR FIDVR ANALYSIS

by

Zhongyi Xia

A thesis submitted in partial fulfillment of the requirement for the degree of

Master of Science

(Electrical Engineering)

At the

**University of Wisconsin - Madison**

2017

**Approved by**

Advisor Signature: [signature]

Advisor Title: Professor

Date: May 4, 2017

# Abstract

The main focus of this research is dynamic load modeling for Fault Induced Delayed Voltage Recovery (FIDVR). FIDVR is the phenomenon whereby the system voltage remains at uncontrolled reduced levels for several seconds after fault in the system has been cleared. When FIDVR happens, the load loss due to motor protective device is significant, and subsequently leads to over voltage.

The stalling of the motors in air-conditioners is believed to be one of the causes of FIDVR, so building a dynamic model for the motor and load to simulate the stall behavior during voltage fault is necessary. The air-conditioner unit consists of a two-phase induction motor and a compressor load. The first step is to model the two-phase induction motor with rotation field theory. Afterwards, a dynamic phasor model is developed and used to match the behavior observed during tests. The load torques of different compressor loads are studied. The load torque and moment of inertia variation due to gas pressure is modeled to better characterize the stall behavior of the motor.

A regression parameter estimation model is constructed to estimate the machine parameters to match the simulation and measurement data. The model is built so that the simulation result can match the current and voltage waveforms for different operation conditions. Most importantly, the model is able to match the stall behavior for different voltage fault situations and predict the stall behavior for cases that are not tested in the lab for future use.

# Acknowledgements

First of all, I wish to thank Professor Lesieutre for offering me the chance to work on such an interesting project, and his continual help and guidance during my master's degree. It's a wonderful experience to apply the knowledge I learned through class and research meetings to a project like this and I really enjoy it.

Secondly, I would like to thank all the professors at University of Wisconsin-Madison who have taught me so much during my graduate study. Without those knowledge, I would not be able to finish my research project.

I would like to gratefully acknowledge support for a graduate research assistantship from the U.S. Department of Energy through the Consortium for Electric Reliability Technology Solutions (CERTS), and the Power System Engineering Research Center (PSERC).

Finally, I would like to thank my parents for their support in every decision I made.

Thank you all.

# Table of Contents

# List of Figures

# List of Tables

# Nomenclature

| Symbol | Description |
|---|---|
| $\theta, \Theta$ | angular position |
| $\omega, \Omega$ | angular velocity |
| $\omega_r$ | rotor electrical velocity |
| $\theta_r$ | rotor electrical position |
| $T_L$ | Load torque |
| $T_{em}$ | electro-mechanical torque |
| $p$ | differentiation |
| $P$ | machine pole number |
| $J$ | moment of inertia |

**Superscripts**

| | |
|---|---|
| $()'$ | variable referred to stator side |

**Subscripts**

| | |
|---|---|
| $( )_s$ | Stator (Main Winding) |
| $( )_S$ | Stator (Auxiliary Winding) |
| $( )_r$ | Rotor |
| $( )_{sr}$ | Mutual (Main Winding) |
| $( )_{Sr}$ | Mutual (Auxiliary Winding) |

**Abbreviations**

| | |
|---|---|
| FIDVR | Fault Induced Delayed Voltage Recovery |

# Chapter 1 *Introduction &Literature Review*

## Research Motivation

The North American Electric Reliability Corporation (NERC) held a Technical Workshop on Dynamic Load Modeling and Fault Induced Delayed Voltage Recovery (FIDVR) in September 2015, which highlighted the current state-of-the-art in dynamic load modeling and the motor testing and simulation studies performed that provide the technical basis for the current dynamic load models. The workshop highlighted the composite load model and the physical nature of end-use loads that drive the various components of the model including induction motor load.

This research focuses on the load model for induction motors with compressor load used in HVAC application that impacts Fault Induced Delayed Voltage Recovery events.

Two-phase induction motors in residential air conditioners are believed to be the cause of prolonged voltage dips in the Southwest, Florida, and likely elsewhere. During these events, a short fault (properly cleared) cause these motors to stall. In most cases, these events are self-correcting, and do not cause customer load interruptions. However, sometimes the motor would not restart itself causing delayed voltage recovery. A typical FIDVR event may cause some local distribution circuit trips and consequential customer load

interruptions. There is also a concern that FIDVR events could have detrimental impacts to the grid such as blackouts, generation tripping and regional voltage instability. [20]

It is desired to develop a dynamic model for compressor-driving two-phase induction motors to simulate the behavior of the motor during voltage fault, so that the stall behavior of the motor-compressor AC unit can be predicted. Thus, further study on how the stalling of motor impact FIDVR can be performed.

## 1.1 Fault Induced Delayed Voltage Recovery (FIDVR)

In areas of warm climates, the power consumption is mainly due to the demand of air conditioner loads. In these areas, the faults on hot days can cause the stalling of motors in A/C loads, resulting in Fault Induced Delayed Voltage Recovery (FIDVR) events. A typical FDIVR event is shown in Fig 1.1 [21].

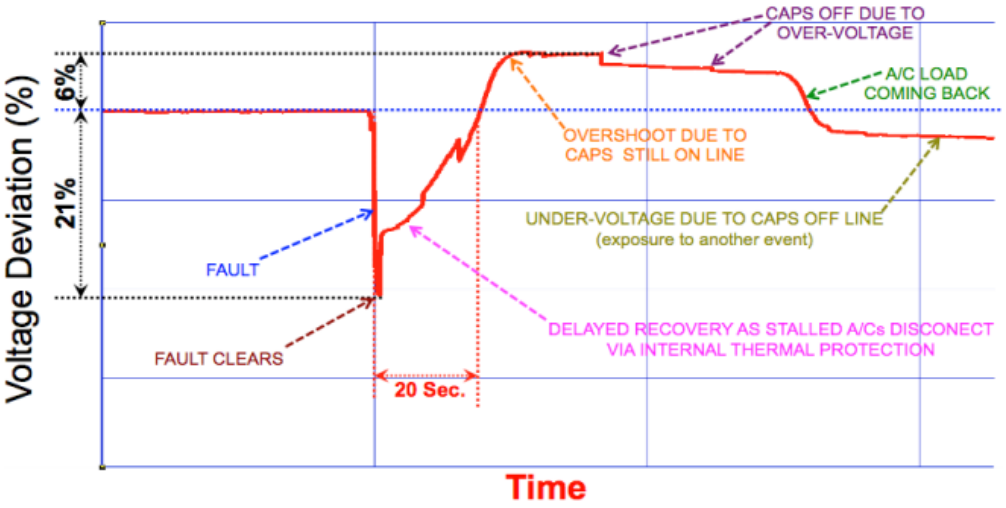


Fig. 1.1 Typical FIDVR event characteristics [21]

A typical FIDVR event has the following anatomy [21]:

Fault: typically caused by accidents, equipment failure, or natural events, which depressed the voltage to the point where A/C motor stalling may occur.

Fault clearance: faulted area is isolated from the system by normal relay protection mechanisms.

Voltage suppression: A/C stalling quickly changes real and reactive power demand causing the voltage not to recover fully.

Slow voltage recovery: induction motor thermal protection disconnects stalled A/C units from the grid allowing voltage to recover.

Overvoltage: caused by the loss of load and large numbers of system capacitors turned on because of high system load conditions before the fault.

Undervoltage: caused by two factors – automatic disconnection of system capacitors due to high system voltages and automatic reconnection of load back onto the system. This Undervoltage could cause another series of similar, possibly worse system disturbances if additional faults occur prior to the system returning to normal voltage.

System normalization: caused by generation responding to load change conditions and voltage stabilization to normal values.

As stated in [21], a FIDVR event could have detrimental impacts to the grid, and it is mainly caused by the stalling of A/C load. The modeling of A/C loads is essential to study FIDVR. A two-phase induction motor with compressor load is widely used in the U.S. Thus, the detailed modeling of two-phase induction motors is also studied.

## 1.2 Two-Phase Induction Motor model in ab-Coordinates

The motor used in an air conditioning unit studied is a two-phase induction motor with a capacitor connecting the excitation voltage and the auxiliary winding as shown in Fig. 1.2.

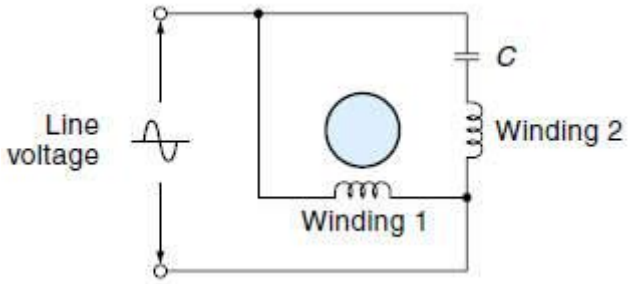


Fig. 1.2 The two-phase induction machine conceptual diagram

The usual orientation of axes of the machine in ab-coordinates is shown in Fig. 1.3 [1]

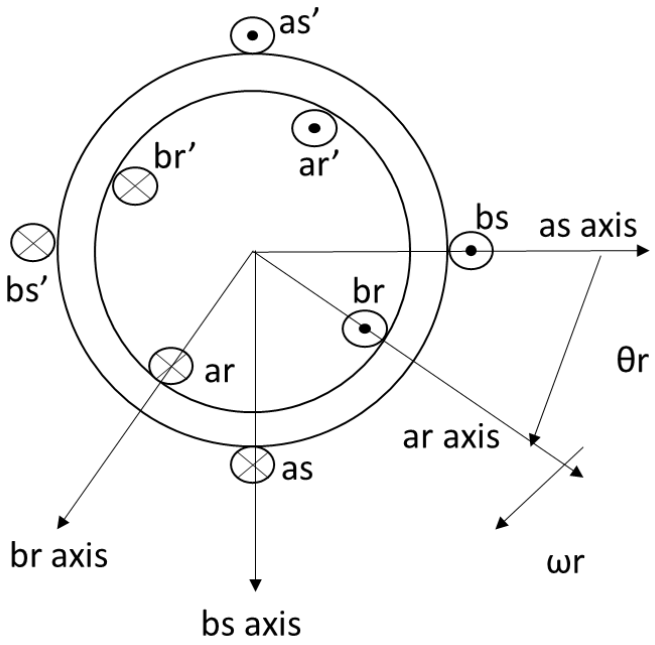


Fig. 1.3 ab-coordinate for two pole two-phase induction machine [1]

The main winding is the stator winding that is mainly used to produced torque. However, at zero speed the sinusoidal voltage applied to the stator winding will cause two equal air-gap magnetomotive force(MMF) in opposite direction, resulting in zero average torque at zero rotor speed. With only one stator winding the motor cannot start rotating itself. Thus,

the auxiliary winding is placed in quadrature to the main winding and connect to the source voltage with a capacitor to create a leading current in the auxiliary winding, allowing the motor to start itself. In steady state the capacitor-connected auxiliary winding also contributes to torque.

The machine variables such as the current and voltage inside the machine can be calculated with basic machine equations (1.1) and (1.2)

$$\mathbf{v}_{\text{abs}} = \mathbf{r}_{\text{s}}\mathbf{i}_{\text{abs}} + \frac{d\boldsymbol{\lambda}_{\text{abs}}}{dt} \tag{1.1}$$

$$\mathbf{v}_{\text{abr}} = \mathbf{r}_{\text{r}}\mathbf{i}_{\text{abr}} + \frac{d\boldsymbol{\lambda}_{\text{abr}}}{dt} \tag{1.2}$$

where

$$\mathbf{f}_{\text{ab}} = [f_a \; f_b]^T \tag{1.3}$$

$$\mathbf{r}_{\text{s}} = \text{diag}[r_s \; r_S] \tag{1.4}$$

$$\mathbf{r}_{\text{r}} = \text{diag}[r_r \; r_r] \tag{1.5}$$

The vector with subscripts ab means it is a vector than contains variable from both a-axis and b-axis. $r_s$ represents a-axis, which is the main winding, stator resistance while $r_S$ is the b-axis, auxiliary, stator resistance. The flux linkage term $\boldsymbol{\lambda}$ in (1.1) can be expressed as:

$$\begin{bmatrix}\boldsymbol{\lambda}_{\text{abs}}\\ \boldsymbol{\lambda}_{\text{abr}}\end{bmatrix}=\begin{bmatrix}\mathbf{L}_{\text{s}} & \mathbf{L}_{\text{sr}}\\ (\mathbf{L}_{\text{sr}})^{T} & \mathbf{L}_{\text{r}}\end{bmatrix}\begin{bmatrix}\mathbf{i}_{\text{abs}}\\ \mathbf{i}_{\text{abr}}\end{bmatrix} \tag{1.6}$$

where:

$$\mathbf{L}_{\text{s}}=\begin{bmatrix}L_{ls}+L_{ms} & 0\\ 0 & L_{lS}+L_{mS}\end{bmatrix} \tag{1.7}$$

$$\mathbf{L}_{\text{r}}=\begin{bmatrix}L_{lr}+L_{mr} & 0\\ 0 & L_{lr}+L_{mr}\end{bmatrix} \tag{1.8}$$

$$\mathbf{L}_{\text{sr}}=\begin{bmatrix}L_{sr}\cos\theta_r & -L_{sr}\sin\theta_r\\ L_{Sr}\sin\theta_r & L_{Sr}\cos\theta_r\end{bmatrix} \tag{1.9}$$

$$L_{sr}=\frac{N_r}{N_s}L_{ms} \tag{1.10}$$

$$L_{Sr}=\frac{N_r}{N_S}L_{mS} \tag{1.11}$$

$L_{ls}$ and $L_{ms}$ are the leakage inductance and magnetizing inductance for main winding (as winding), while $L_{lS}$ and $L_{mS}$ are those for auxiliary winding (bs winding). $L_{sr}$ and $L_{Sr}$ are the cross-coupling mutual inductance between the stator windings and rotor windings. The actual magnitude of the mutual inductance is dependent on the stator-rotor turns ratio and position of the rotor, as shown in (1.9) - (1.11).

The expression of electromagnetic torque can be described by:

$$T_e=\left(\frac{P}{2}\right)(\mathbf{i}_{\text{abs}})^{T}\frac{\partial}{\partial\theta_r}(\mathbf{L}_{\text{sr}})^{T}\mathbf{i}_{\text{abr}} \tag{1.12}$$

$$T_e = \left(\frac{P}{2}\right)[L_{sr} i_{as}(-i_{ar}\sin\theta_r - i_{br}\cos\theta_r) + L_{Sr} i_{bs}(i_{ar}\cos\theta_r - i_{br}\sin\theta_r)] \quad (1.13)$$

$$T_e - T_L = J\left(\frac{2}{P}\right)p\omega_r \quad (1.14)$$

## 1.3 Two-Phase Induction Motor Model in dq-Coordinates

The rotor variables of the two-phase induction motor are now transformed into a dq reference frame coordinate as shown in Fig. 1.4. In (1.9) the mutual inductances are dependent on the position of the rotor. By transforming into dq reference frame coordinates, the position dependence is removed and a frame dependent back-emf term is introduced to the machine equation (1.18). The benefit of transforming into dq coordinate is that we can now choose our own reference frame instead of staying at stationary frame of ab coordinates. We can transform into synchronous frame by rotating the reference frame with excitation frequency. The AC current and voltage in the motor becomes DC when viewed in the synchronous frame. It is easier to study the steady state performance in the synchronous frame. [5]

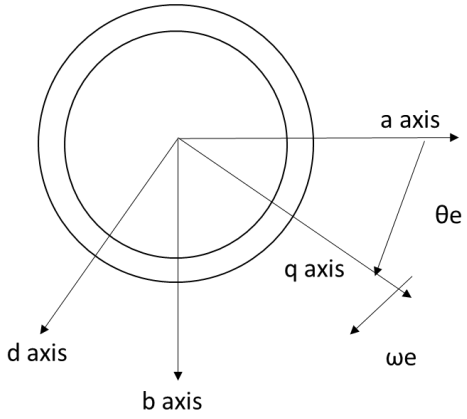


Fig. 1.4 Conceptual Diagram of Reference Frame Transformation

Then the machine equation in ab-coordinate are converted to dq-coordinates with (1.15)

$$f_{qds} = \begin{bmatrix} cos\theta & sin\theta \\ sin\theta & -cos\theta \end{bmatrix} f_{abs} \tag{1.15}$$

where $\theta$ is the reference frame position.

After the transformation, the machine equations become:

$$v_{qs} = r_s i_{qs} + \frac{d\lambda_{qs}}{dt} \tag{1.16}$$

$$v_{ds} = r_S i_{ds} + \frac{d\lambda_{ds}}{dt} \tag{1.17}$$

$$v_{qr} = r_r i_{qr} - \omega\lambda_{dr} + \frac{d\lambda_{qr}}{dt} \tag{1.18}$$

$$v_{dr} = r_r i_{dr} + \omega\lambda_{qr} + \frac{d\lambda_{dr}}{dt} \tag{1.19}$$

where the dq axis flux linkage:

$$\lambda_{qs} = L_{ls} i_{qs} + L_{ms} i_{qs} + L_{sr} i_{qr}$$

$$\lambda_{ds} = L_{lS} i_{ds} + L_{mS} i_{ds} + L_{Sr} i_{dr} \quad (1.20)$$

$$\lambda_{qr} = L_{lr} i_{qr} + L_{sr} i_{qs} + L_{mr} i_{qr} \quad (1.21)$$

$$\lambda_{dr} = L_{lr} i_{dr} + L_{Sr} i_{ds} + L_{mr} i_{dr} \quad (1.22)$$

(1.23)

When developing an equivalent circuit of the electric machine, rotor variables are referred to stator windings by a turns ratio. For the unsymmetrical two phase machine, the turns ratio for main winding and auxiliary winding are different. So the q-axis variable are all referred to the main winding with turns ratio of Ns, and the d-axis variables are referred to the auxiliary winding with turns ratio of NS.

$$v_{qs} = r_s i_{qs} + \frac{d\lambda_{qs}}{dt} \quad (1.24)$$

$$v_{ds} = r_S i_{ds} + \frac{d\lambda_{ds}}{dt} \quad (1.25)$$

$$v'_{qr} = r'_r i_{qr} - \frac{N_s}{N_S} \omega \lambda'_{dr} + \frac{d\lambda'_{qr}}{dt} \quad (1.26)$$

$$v'_{dr} = r'_r i_{dr} + \frac{N_S}{N_s} \omega \lambda'_{qr} + \frac{d\lambda'_{dr}}{dt} \quad (1.27)$$

Where

$$\lambda_{qs} = L_{ls} i_{qs} + L_{ms}\left(i_{qs} + i'_{qr}\right) \quad (1.28)$$

$$\lambda_{ds} = L_{lS} i_{ds} + L_{mS}(i_{ds} + i'_{dr}) \quad (1.29)$$

$$\lambda'_{qr} = L'_{lr} i'_{qr} + L_{ms}(i_{qs} + i'_{qr}) \quad (1.30)$$

$$\lambda'_{dr} = L'_{lR} i'_{dr} + L_{mS}(i_{ds} + i'_{dr}) \quad (1.31)$$

Table 1.1 shows how the variable are referred to stator windings.

Table 1.1 The machine variables referred to stator windings

| | | |
|---|---|---|
| $v'_{qr} = \frac{N_s}{N_r} v_{qr}$ | $i'_{qr} = \frac{N_r}{N_s} i_{qr}$ | $v'_{dr} = \frac{N_S}{N_r} v_{dr}$ |
| $i'_{dr} = \frac{N_r}{N_S} i_{dr}$ | $r'_r = \left(\frac{N_s}{N_r}\right)^2 r_r$ | $L'_{lr} = \left(\frac{N_s}{N_r}\right)^2 L_{lr}$ |
| $r'_R = \left(\frac{N_S}{N_r}\right)^2 r_r$ | $L'_{lR} = \left(\frac{N_S}{N_r}\right)^2 L_{lr}$ | $L_{ms} = \frac{N_s}{N_r} L_{sr}$ |
| $L_{mS} = \frac{N_S}{N_r} L_{Sr}$ | | |

It is often convenient to express the voltage and flux linkage in terms of reactance instead of inductance. Equations (1.28-1.31) become

$$v_{qs} = r_s i_{qs} + \frac{1}{\omega_b} \frac{d\psi_{qs}}{dt} \quad (1.32)$$

$$v_{ds} = r_S i_{ds} + \frac{1}{\omega_b} \frac{d\psi_{ds}}{dt} \quad (1.33)$$

$$v'_{qr} = r'_r i_{qr} - \frac{N_s}{N_S}\frac{\omega}{\omega_b}\psi'_{dr} + \frac{1}{\omega_b}\frac{d\psi'_{qr}}{dt} \tag{1.34}$$

$$v'_{dr} = r'_R i_{dr} + \frac{N_S}{N_s}\frac{\omega}{\omega_b}\psi'_{qr} + \frac{1}{\omega_b}\frac{d\psi'_{dr}}{dt} \tag{1.35}$$

$$\psi_{qs} = X_{ls} i_{qs} + X_{ms}\left(i_{qs} + i'_{qr}\right) \tag{1.36}$$

$$\psi_{ds} = X_{lS} i_{ds} + X_{mS}(i_{ds} + i'_{dr}) \tag{1.37}$$

$$\psi'_{qr} = X'_{lr} i'_{qr} + X_{ms}\left(i_{qs} + i'_{qr}\right) \tag{1.38}$$

$$\psi'_{dr} = X'_{lR} i'_{dr} + X_{mS}(i_{ds} + i'_{dr}) \tag{1.39}$$

$$\begin{bmatrix} v_{qs} \\ v_{ds} \\ v'_{qr} \\ v'_{dr} \end{bmatrix} = \begin{bmatrix} r_s + \frac{X_{ss}}{\omega_b}p & 0 & \frac{X_{ms}}{\omega_b}p & 0 \\ 0 & r_s + \frac{X_{ss}}{\omega_b}p & 0 & \frac{X_{mS}}{\omega_b}p \\ \frac{1}{\omega_b}\frac{dX_{ms}}{dt} & -\frac{1}{n}\frac{\omega_r}{\omega_b}X_{ms} & r'_r + \frac{X'_{rr}}{\omega_b}p & -\frac{1}{n}\frac{\omega_r}{\omega_b}X'_{RR} \\ n\frac{\omega_r}{\omega_b}X_{mS} & \frac{X_{mS}}{\omega_b}p & n\frac{\omega_r}{\omega_b}X'_{rr} & r'_R + \frac{X'_{RR}}{\omega_b}p \end{bmatrix} \begin{bmatrix} i_{qs} \\ i_{ds} \\ i'_{qr} \\ i'_{dr} \end{bmatrix} \tag{1.40}$$

where p denotes time derivative d/dt.

Table 1.2 Variable Notation used in Equation (1.40)

| | |
|---|---|
| $X_{ss} = X_{ls} + X_{ms}$ | $X_{SS} = X_{lS} + X_{mS}$ |
| $X'_{rr} = X'_{lr} + X_{ms}$ | $X'_{RR} = X'_{lR} + X_{ms}$ |
| $n = \frac{N_S}{N_s}$ | |

The electromagnetic torque can be expressed in:

$$T_e = \left(\frac{P}{2}\right)\left(\frac{N_S}{N_s}\right)\left(\frac{X_{ms}}{\omega_b}\right)\left(i_{qs}i'_{dr} - i_{ds}i'_{qr}\right) \tag{1.41}$$

Fig. 1.5 shows the machine variable waveform when using the model in this section for a capacitor-start capacitor-run motor (from [1]).

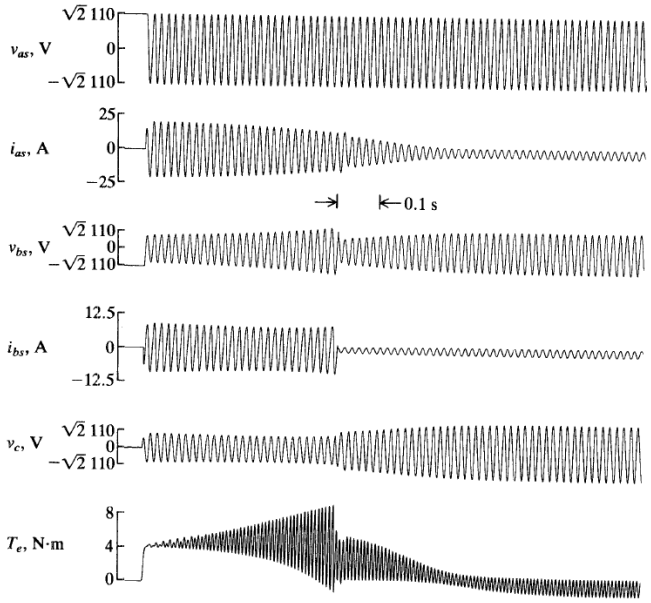


Fig. 1.5 Machine Variable Waveform Simulation Results [1]

During start up transient, the main winding current $i_{as}$ and auxiliary winding current $i_{bs}$ are large to produce the larger electro-magnetic torque to overcome the load torque and produce positive net torque to accelerate the motor. After motor approaches rated speed, the start capacitor is disconnected leaving the run capacitor connected. The current decrease gradually, until the motor reaches rated speed. Then the currents become small making the electro-magnetic torque equals the load torque, and the motor reaches steady state.

## 1.4 Point on Wave Model

The "point-on-wave" model is the transient model based on the ab-coordinates theory and the basic machine differential equations:

$$\frac{\partial \lambda_{as}}{\partial t} = v_{as} - r_s i_{as} \tag{2.1}$$

$$\frac{\partial \lambda_{bs}}{\partial t} = v_{bs} - r_S i_{bs} \tag{2.2}$$

$$\frac{\partial \lambda_{ar}}{\partial t} = v_{ar} - r_r i_{ar} \tag{2.3}$$

$$\frac{\partial \lambda_{br}}{\partial t} = v_{br} - r_r i_{br} \tag{2.4}$$

$$\frac{\partial \omega_r}{\partial t} = \frac{1}{J}(T_e - T_L) \tag{2.5}$$

It is called the point on wave model, since this method presents the complete detailed information about the machine variable waveform at each time point during an electrical cycle. Compared with Dynamic Phasor Model, the point on wave model focus more on the detailed waveform, so that it is able to show the behavior of the motor within one cycle. Thus, we can study the fast transient behavior with this model. The simulation result of the waveform of the motor during a startup transient with rated load is shown in Fig 1.6-Fig 1.8. And the parameters used for the simulation is shown in Table 1.3.

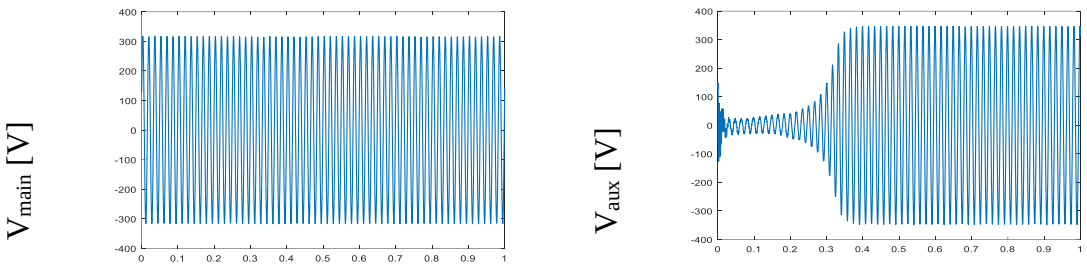


Fig 1.6 Transient Voltage Response During Startup of the Point on Wave Model with rated load. (a) $V_{main}$, (b) $V_{aux}$

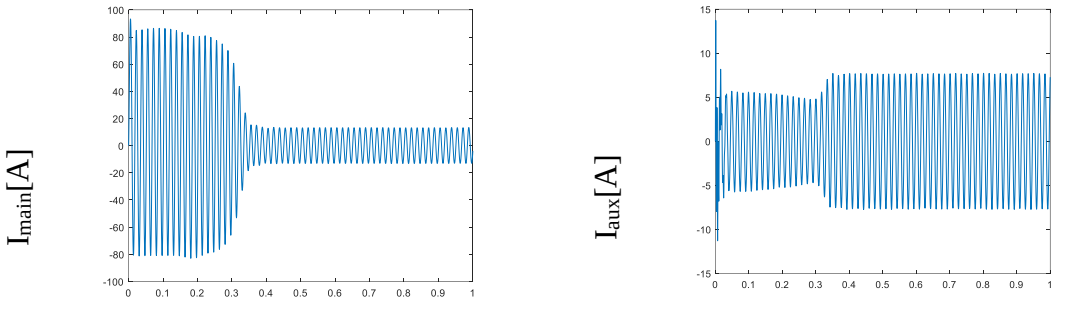


Fig 1.7 Transient Current Response During Startup of the Point on Wave Model with rated load. (a) $I_{main}$, (b) $I_{aux}$

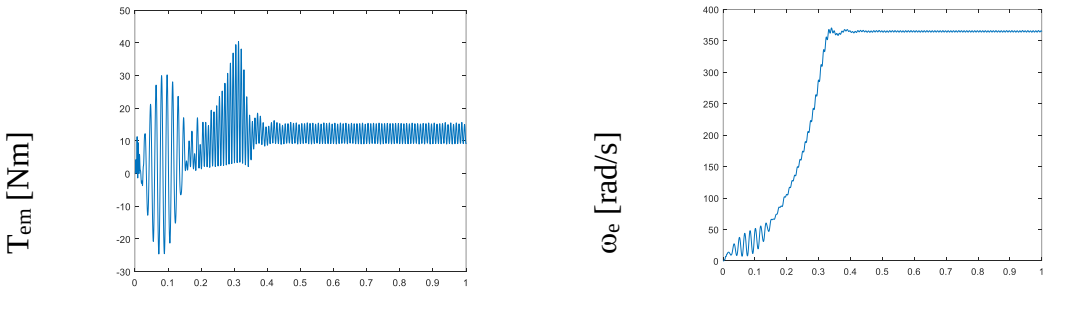


Fig 1.8 Transient Torque and Velocity Response During Startup of the Point on Wave Model with rated load. (a) $T_{em}$, (b) $\omega_e$

| Table 1.3 Machine Parameters for Point on Wave Simulation | | | |
|---|---|---|---|
| Parameter | Symbol | Value | Unit |
| Main Winding Stator Resistance | $R_s$ | 1.2 | [Ω] |
| Auxiliary Winding Stator Resistance | $R_S$ | 2.2 | [Ω] |
| Rotor Resistance | $R_r$ | 1.1 | [Ω] |
| Main Winding Leakage Inductance | $L_{ls}$ | 3.1 | [mH] |
| Auxiliary Winding Leakage Inductance | $L_{lS}$ | 4.7 | [mH] |
| Rotor Leakage Inductance | $L_{lr}$ | 3.4 | [mH] |
| Main Winding Magnetizing Inductance | $L_{ms}$ | 104.8 | [mH] |
| Auxiliary Winding Magnetizing Inductance | $L_{mS}$ | 139.5 | [mH] |

## 1.5 Dynamic Phasor Model

The main idea of the dynamic phasor model is to approximate the time domain x(τ) in the interval τ ∈ (t−T,t] with a Fourier series

$$x(\tau) = \sum_{k=-\infty}^{\infty} X^k(t)\, e^{jkw_b\tau} \tag{1.42}$$

where the $X^k(t)$ are the k-th complex Fourier coefficient at time t determined by:

$$X^k(t) = \frac{1}{T}\int x(\tau)\, e^{-jkw_b\tau} d\tau = \langle x \rangle_k(t) \tag{1.43}$$

In this approach, simulating induction machine yields an envelope over the ac waveforms as shown in Fig. 1.9 [3]

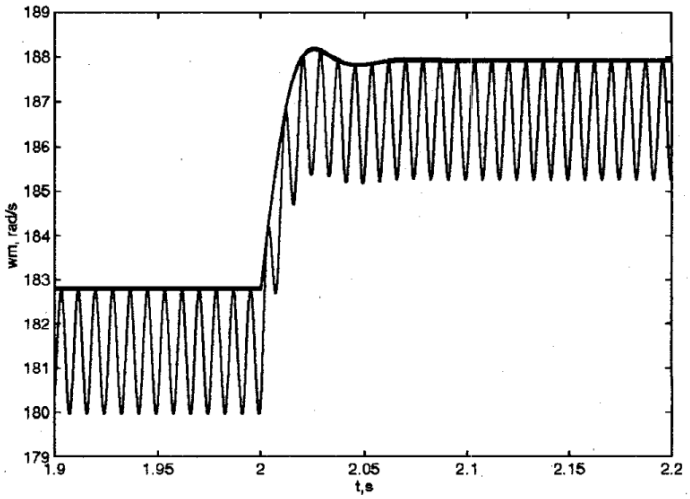


Fig. 1.9 Dynamic Phasor model compared with point on wave model [3]

The dq reference frame coordinate can be used to model the dynamic phasor model. Then all electrical variable can be represented by fundamental frequency phasors.

$$i_{ds} = \sqrt{2} I_{ds}^{R} \cos(\omega_b t + \phi) - \sqrt{2} I_{ds}^{I} \sin(\omega_b t + \phi) \tag{1.44}$$

$$= \frac{1}{\sqrt{2}} (I_{ds}^{R} - j I_{ds}^{I}) e^{-j(\omega_b t + \phi)} + \frac{1}{\sqrt{2}} (I_{ds}^{R} + j I_{ds}^{I}) e^{+j(\omega_b t + \phi)}$$

The rotor flux dynamic is transformed into forward- and backward-rotating fields to model the fast dynamics of the machine. Under normal operation the backward rotating field dynamics are fast and can be neglected. Then the magnetizing inductance is adjusted as function of rotor flux for saturation model.

The resulting model is: [2]

$$|V_s| = \left(r_{ds} + j\frac{\omega_s}{\omega_b}X'_{ds}\right)(I^R_{ds} + jI^I_{ds}) + j\frac{X_m}{X_r}(\psi^R_{dr} + j\psi^I_{dr})$$

$$|V_s| = \left(r_{qs} + j\frac{\omega_s}{\omega_b}X'_{qs} + j\frac{\omega_s}{\omega_b}X_c\right)(I^R_{qs} + jI^I_{qs}) + j\frac{\omega_s}{\omega_b}\frac{nX_m}{X_r}(\psi^R_{qr} + j\psi^I_{qr})$$

$$\begin{bmatrix}(\psi^R_f + j\psi^I_f)\\(\psi^R_b + j\psi^I_b)\end{bmatrix} = \left(\frac{1}{2}\right)\begin{bmatrix}1 & -j\\1 & j\end{bmatrix}\begin{bmatrix}(\psi^R_{dr} + j\psi^I_{dr})\\(\psi^R_{qr} + j\psi^I_{qr})\end{bmatrix}$$

$$\begin{bmatrix}(\psi^R_{dr} + j\psi^I_{dr})\\(\psi^R_{qr} + j\psi^I_{qr})\end{bmatrix} = \begin{bmatrix}1 & 1\\j & -j\end{bmatrix}\begin{bmatrix}(\psi^R_f + j\psi^I_f)\\(\psi^R_b + j\psi^I_b)\end{bmatrix}$$

$$\begin{bmatrix}(I^R_f + jI^I_f)\\(I^R_b + jI^I_b)\end{bmatrix} = \left(\frac{1}{2}\right)\begin{bmatrix}1 & -jn\\1 & jn\end{bmatrix}\begin{bmatrix}(I^R_{ds} + jI^I_{ds})\\(I^R_{qs} + jI^I_{qs})\end{bmatrix}$$

$$\begin{bmatrix}(I^R_{ds} + jI^I_{ds})\\(I^R_{qs} + jI^I_{qs})\end{bmatrix} = \begin{bmatrix}1 & 1\\j/n & -j/n\end{bmatrix}\begin{bmatrix}(I^R_f + jI^I_f)\\(I^R_b + jI^I_b)\end{bmatrix}$$

$$T'_o\frac{d}{dt}(\psi^R_f + j\psi^I_f) = X_m(I^R_f + jI^I_f) - \left(sat(\psi_f, \psi_b) + j(\omega_s - \omega_r)T'_o(\psi^R_f + j\psi^I_f)\right)$$

$$(\psi^R_b + j\psi^I_b) = \frac{X_m(I^R_b + jI^I_b)}{\left(sat(\psi_f, \psi_b) + j(\omega_s + \omega_r)T'_o\right)}$$

$$\frac{2H}{\omega_b}\frac{d\omega_r}{dt} = \frac{X_m}{X_r}2\left(I^I_f\psi^R_f - I^R_f\psi^I_f - I^I_b\psi^R_b + I^R_b\psi^I_b\right) - T_{mech}$$

$$I_s = \left[\left((I^R_{ds} + jI^I_{ds})\right) + \left(I^R_{qs} + jI^I_{qs}\right)\right]e^{j\theta}$$

Where：

$$sat(\psi_f, \psi_b) = \begin{cases}1 & \text{for } \psi \le b_{sat}\\1 + A_{sat}(\psi - b_{sat})^2 & \text{for } \psi > b_{sat}\end{cases}$$

And $\psi = \sqrt{\left(\psi^R_f\right)^2 + \left(\psi^I_f\right)^2 + (\psi^R_b)^2 + (\psi^R_b)^2}$

Fig 1.10-Fig. 1.14 shows the simulation result of dynamic phasor model compared with point on wave model during stalling

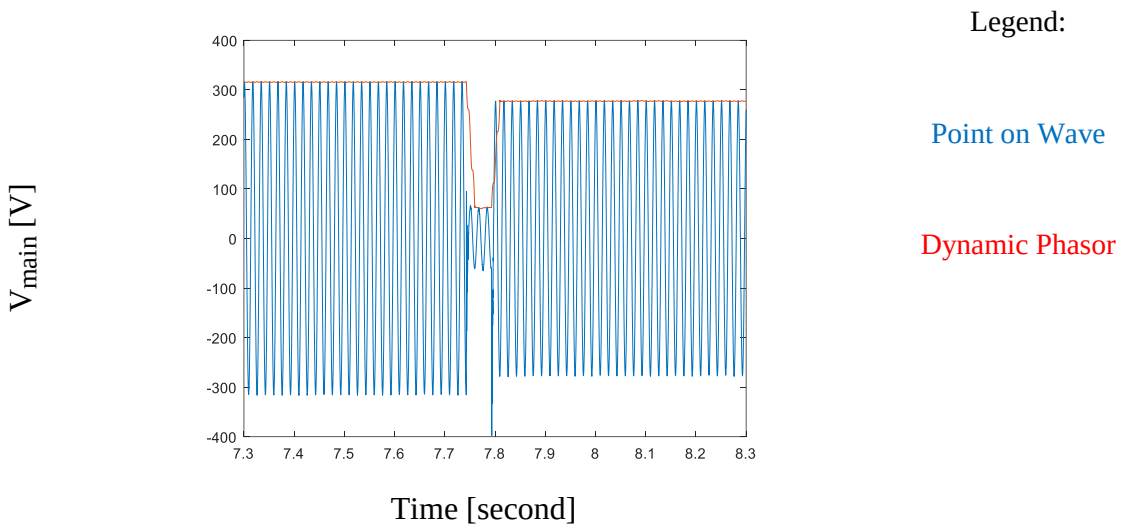


Fig. 1.10 Main Winding Voltage Simulation Waveform Comparison of Point on Wave and Dynamic Phasor Model at stall

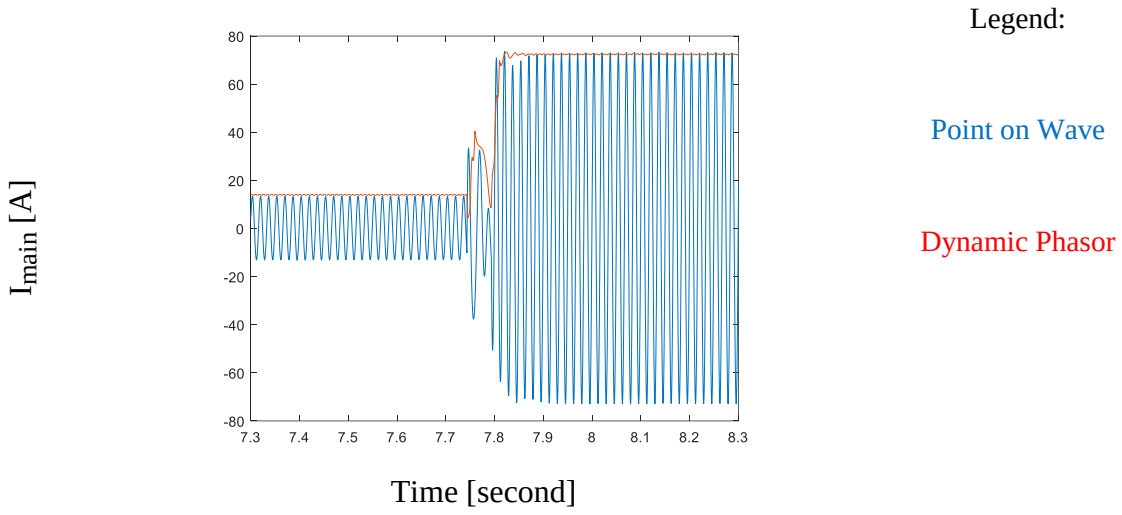


Fig. 1.11 Main Winding Current Simulation Waveform Comparison of Point on Wave and Dynamic Phasor Model at stall

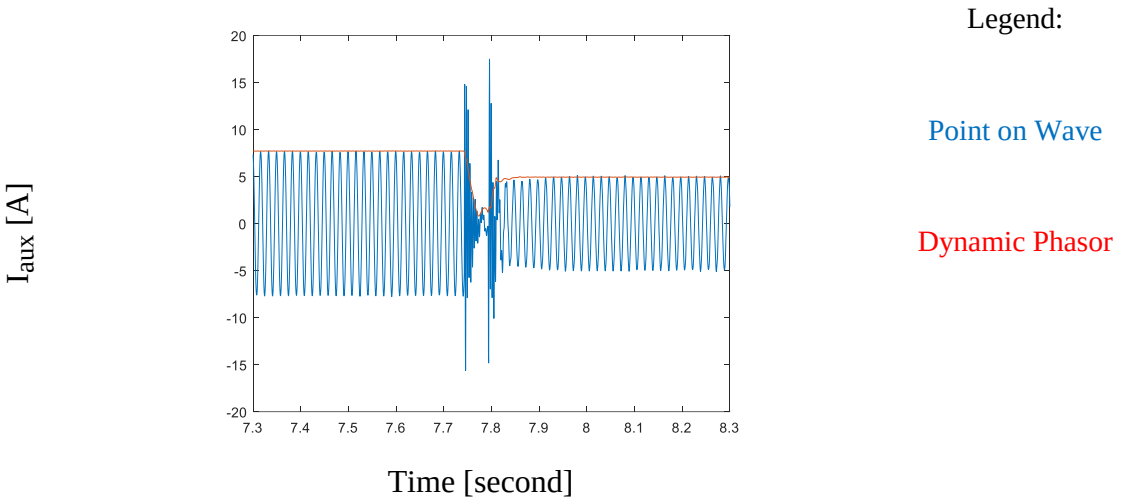


Fig. 1.12 Auxiliary Winding Current Simulation Waveform Comparison of Point on Wave and Dynamic Phasor Model at stall

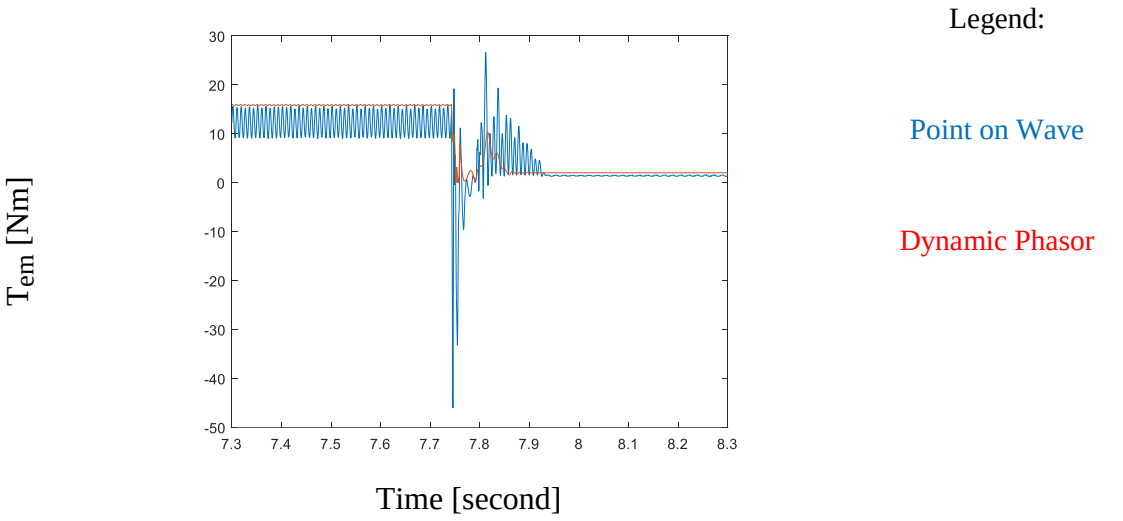


Fig. 1.13 Electro-magnetic Torque Simulation Waveform Comparison of Point on Wave and Dynamic Phasor Model at stall

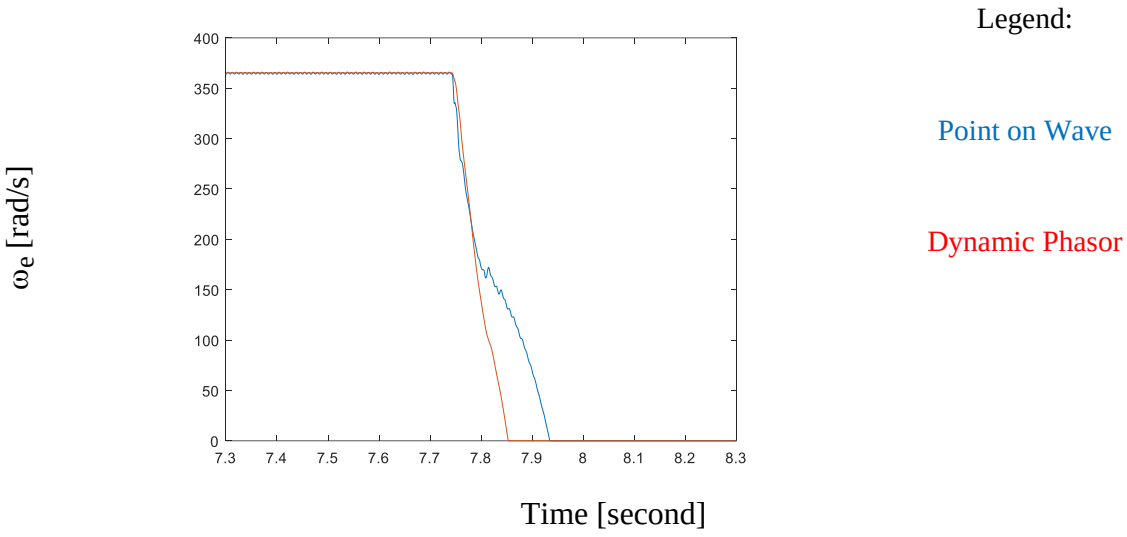


Fig. 1.14 Motor Speed Simulation Waveform Comparison of Point on Wave and Dynamic Phasor Model at stall

The dynamic phasor model is able to track the point on wave model in steady sate. However, it does not capture the sub-cycle dynamics very well since the fast dynamics are neglected. Fig 1.15-Fig 1.19 shows the comparison between two models when the motor does not stall after the fault.

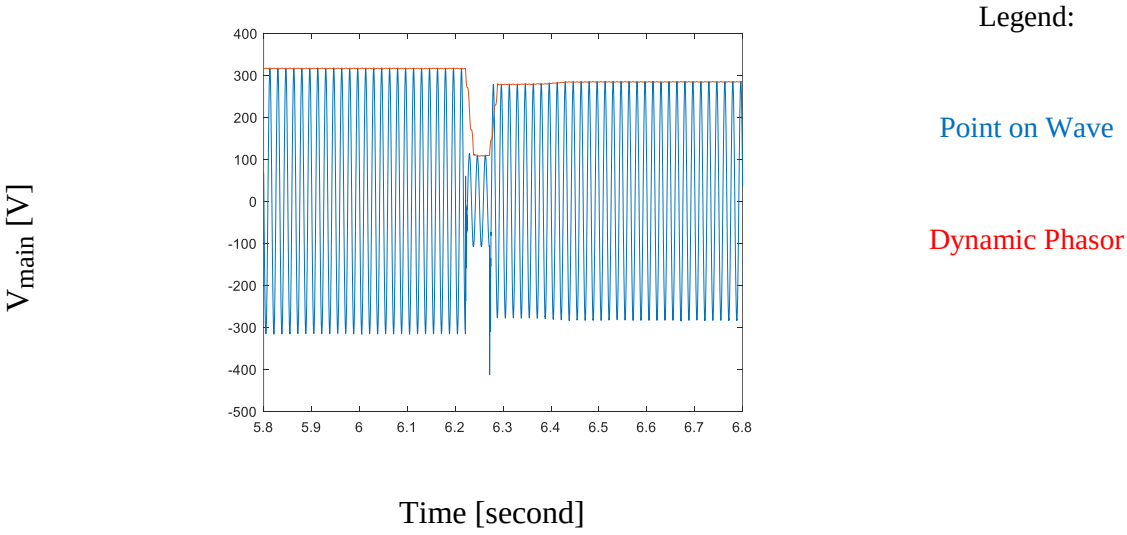


Fig. 1.15 Main Winding Voltage Simulation Waveform Comparison of Point on Wave and Dynamic Phasor Model (no stall)

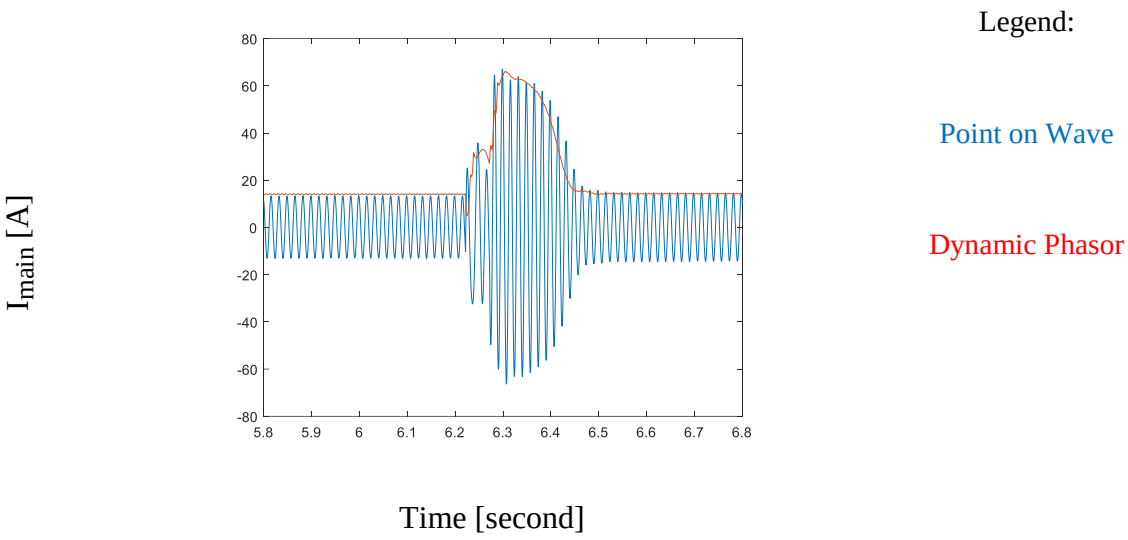


Fig. 1.16 Main Winding Current Simulation Waveform Comparison of Point on Wave and Dynamic Phasor Model (no stall)

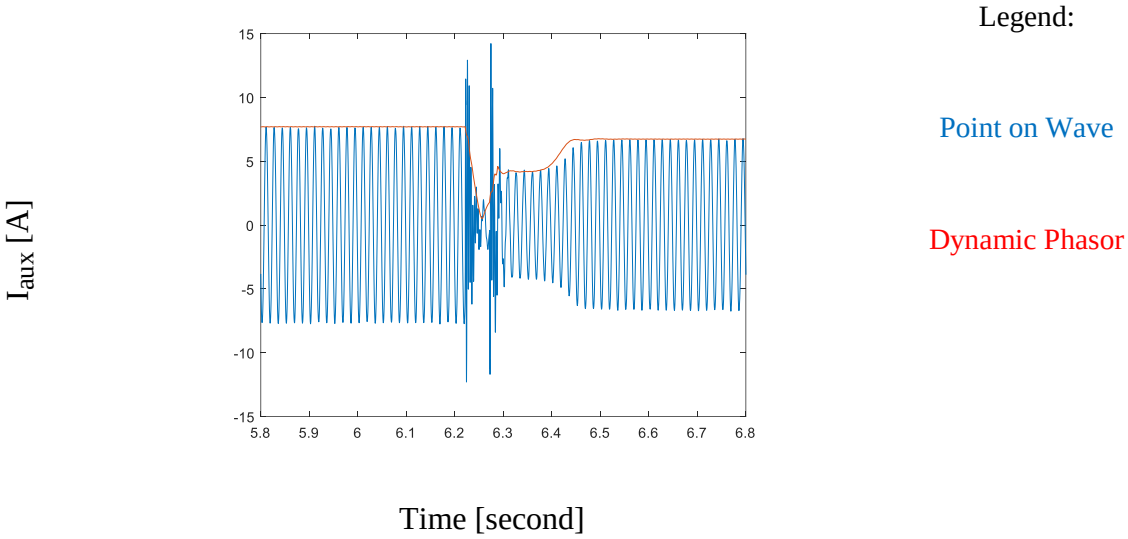


Fig. 1.17 Auxiliary Winding Current Simulation Waveform Comparison of Point on Wave and Dynamic Phasor Model (no stall)

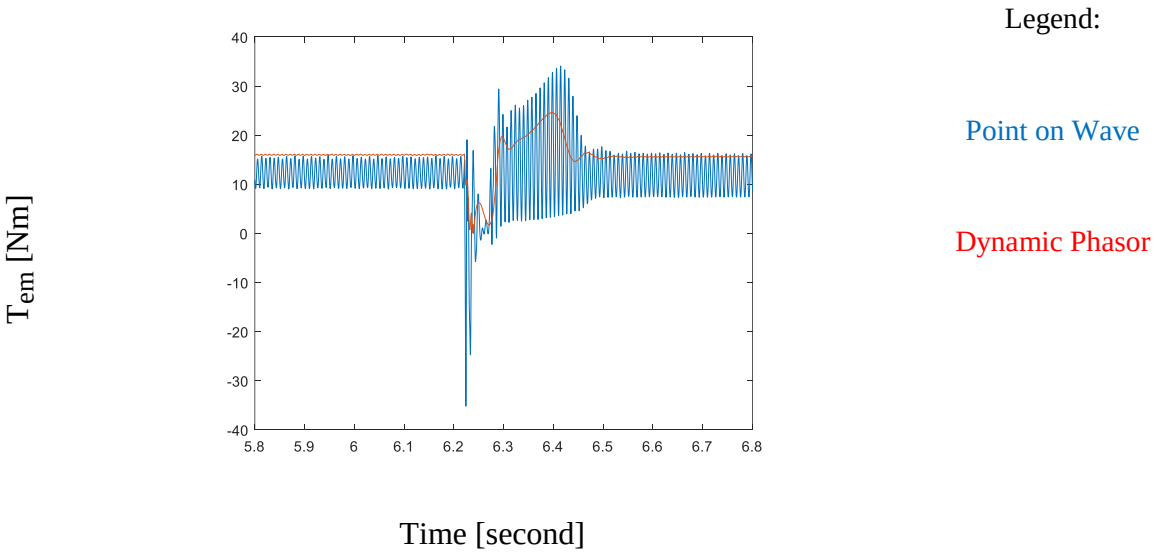


Fig. 1.18 Electro-magnetic Torque Simulation Waveform Comparison of Point on Wave and Dynamic Phasor Model (no stall)

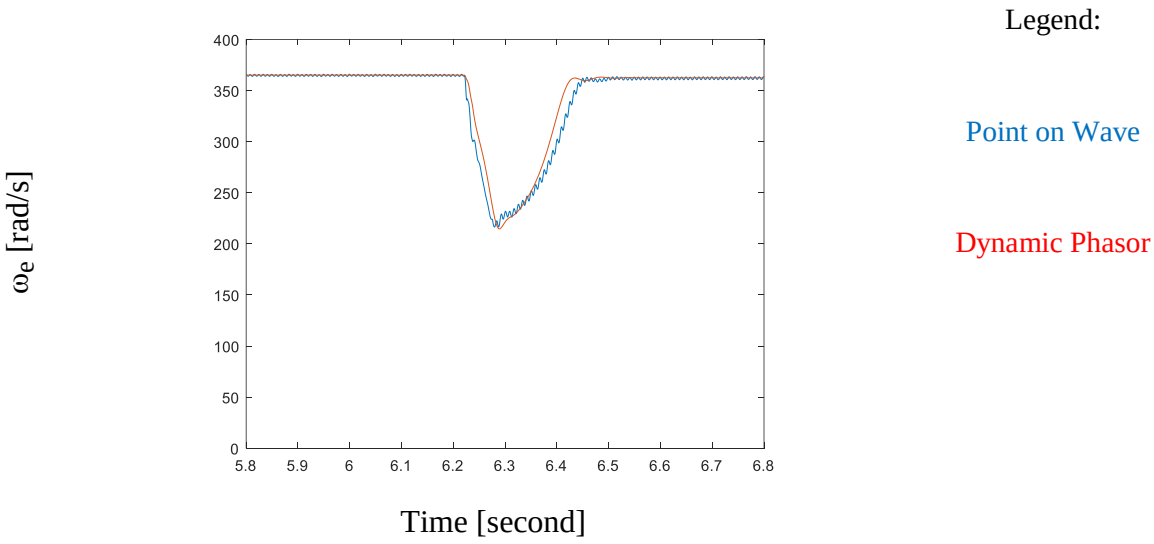


Fig. 1.19 Motor Speed Simulation Waveform Comparison of Point on Wave and Dynamic Phasor Model (no stall)

The simulation result shows that the dynamic phasor model focuses more on the magnitude of the wave form. The dynamic phasor model is desired since it is a positive sequence model which matches with other components in the power system. The tradeoff is that the detailed waveform information within one cycle is lost, so additional adjustments are needed for certain disturbances.

## 1.6 Summary & Research Opportunities

This chapter reviewed the FIDVR caused by the A/C stalling, and presented the models used for modeling the two-phase induction machine. The point on wave model is the conventional that produce the exact waveform of the machine variables. The dynamic phasor model is the desired positive sequence model that works better with other models in the power system. The simulation result of both models is studied and compared. The dynamic phasor model struggles with fast transients. To achieve a more precise model for the machine, additions to the model are presented in next chapter.

The research opportunities identified can be summarized as follows,

- Develop additional mechanical model for the load to capture the stall behavior
- Develop parameter estimation methods to match the simulation with measurements.

## 1.7 Overview of Chapters

Chapter 2 states the model used for modeling the mechanical behavior of the motor-load system.

Chapter 3 introduces the parameter estimation model used to match the measured data with simulation.

Chapter 4 shows the simulation results compared with measured data as well as the stall behavior prediction of the model.

Chapter 5 summarizes this research and suggests future work on this dynamic load modeling for FIDVR analysis.

# Chapter 2 *Compressor Load Modeling*

This chapter introduces the modeling of the compressor load. Firstly, load torques for different compressors are analyzed. Then an additional gas pressure model and a voltage angle model are developed to match the simulation with measurement.

## 2.1 Scroll Compressor as Load

The scroll compressor was invented by Creux [4] in 1905 and if often preferred for its efficiency and smooth operation.

The compressor consists of two interleaving scrolls to pump and compress gas. One of the scrolls is fixed and the other orbits eccentrically without rotating, thereby trapping, pumping and compressing the gas between scrolls. [5][6][7][8][9]

The load torque of the scroll compressor is given by:

$$T = F_\theta \cdot r \tag{2.1}$$

where, $F_\theta$ is the tangential force and is given by:

$$F_\theta = P_s p h \sum_{i=1}^{N} \left(2i - \frac{\theta}{\pi}\right)(p_i - p_{i+1}) \tag{2.2}$$

and i means the i-th chamber, p is the scroll pitch and h is the scroll height, $P_s$ is the suction pressure and $p_i$ is the pressure ratio (= $P_i/P_s$) [10].

The load torque in steady state for an ideal scroll compressor is shown in Fig 2.1 [10].

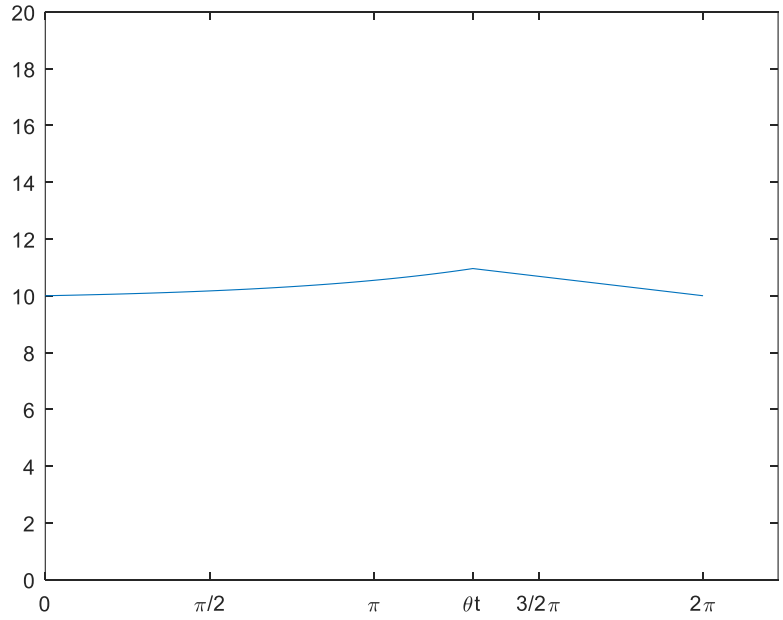


Fig. 2.1 The Load Torque of Scroll Compressor During One Cycle period [10]

As shown in Fig. 2.1, the torque of the scroll compressor increases as the compressor absorbs and compresses the gas. When the orbiting angle reaches $\theta_t$, which is the position that the compressor pumps the gas in the inner most chamber, the torque reaches its maximum and start to decrease.

The load torque of the compressor was initially believed to have a linear relationship with the rotor speed, meaning that at zero speed the load torque should be close to zero so that the motor can start itself after fault is cleared. However, in many cases, the motor keeps stalling even after the fault is cleared. In general, a longer fault duration is more likely to cause the motor to stall. When the fault duration becomes few seconds, the motor can restart itself after the voltage recovers. Fig 2.2 shows a case where the voltage has a 0% fault for 5 seconds, and restarts.

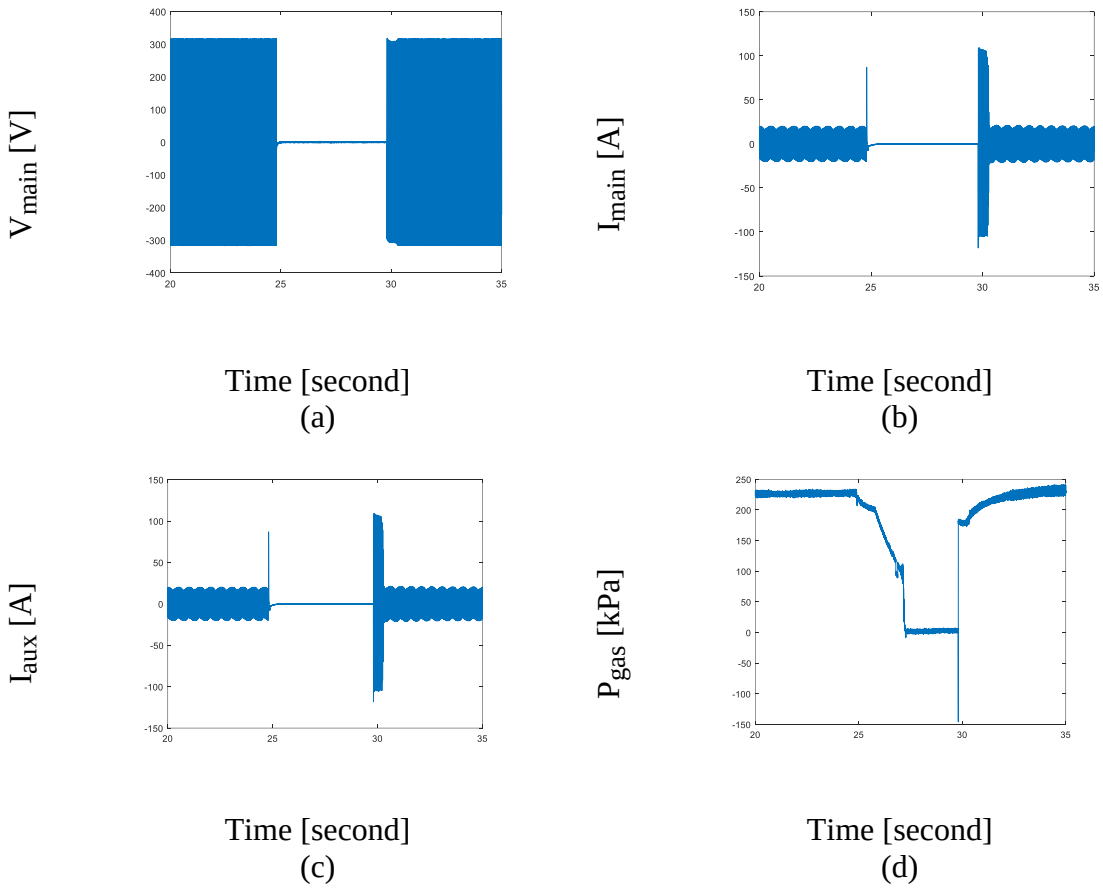


Fig. 2.2 Measured Data for Motor with 0% fault for 5 seconds. (a)$V_{main}$ (b)$I_{main}$ (c)$I_{aux}$ (d)$P_{gas}$

As shown in the Fig. 2.2, a fast depletion of the gas pressure in the A/C unit occurs after few seconds of voltage fault. Then the motor restarts when the voltage recovers. This fact suggests that the load torque may have certain relationship with the gas pressure inside the cell. So the case, where the voltage has 0% fault and recovers gradually in 5 seconds, is studied and shown in Fig 2.3.

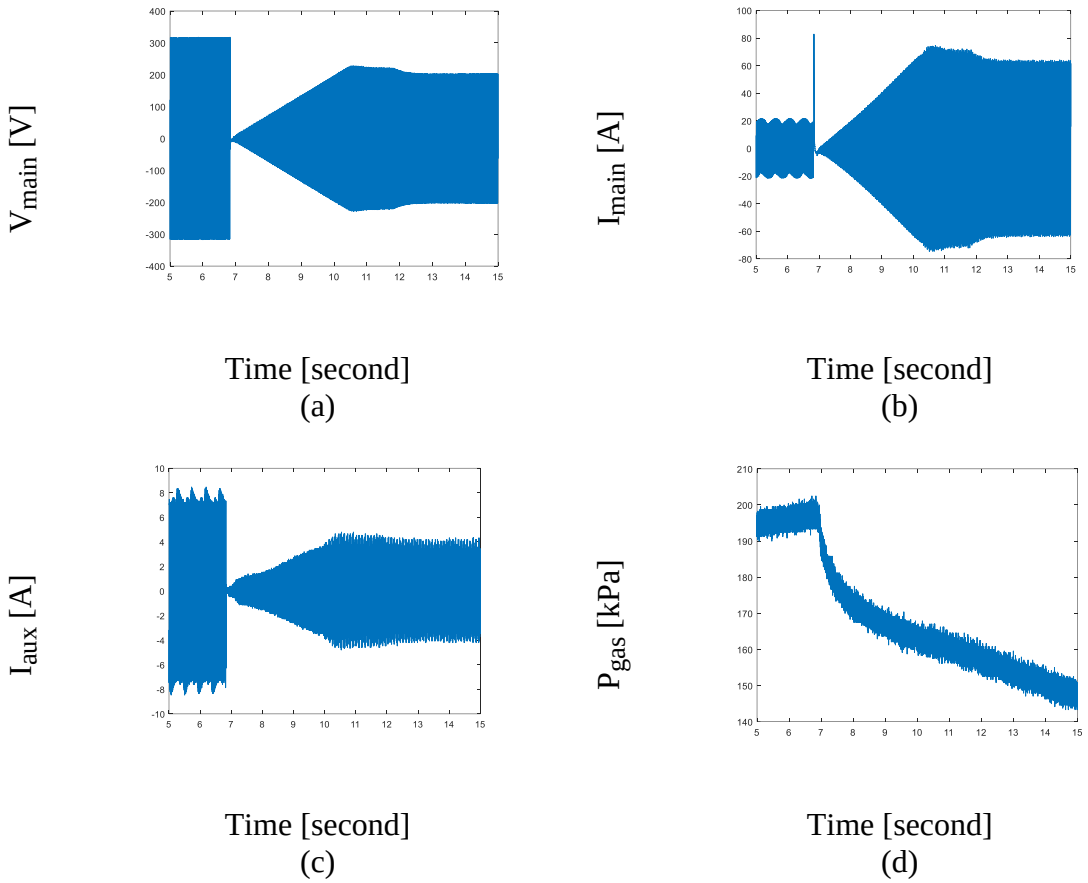


Fig. 2.3 Measured Data for Motor with 0% fault for 5 seconds ramp recovery (a)$V_{main}$ (b)$I_{main}$ (c)$I_{aux}$ (d)$P_{gas}$

As shown in the gas pressure plot in Fig 2.3, it does not have the fast depletion as in Fig 2.2. And the motor keeps stalling after voltage recovers, which leads to an assumption that the load torque is also dependent on the gas pressure. A gas pressure model is presented later in Section 2.3.

## 2.2 Load Torque of Reciprocating Compressor

The reciprocating compressor is also called piston compressor. It uses pistons driven by a crankshaft to deliver gas at high pressure [11].

The load torque of a reciprocating compressor is simulated and shown in Fig 2.4 [12].

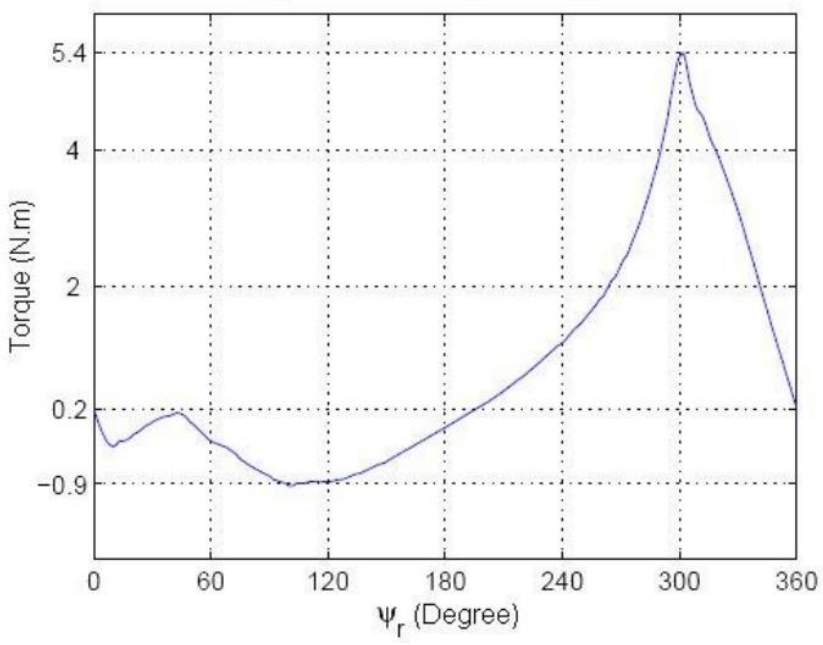


Fig. 2.4 Load Torque of Reciprocating Compress During One Cycle Period. [12]

As shown in the plot, the reciprocating compressor has a much more significant load torque variation than the scroll compressor does. However in the measurement, the reciprocating compressor is observed to have similar load behavior with the scroll compressor, so the gas pressure model developed in Section 2.3 is implemented in both compressors.

## 2.3 Gas Pressure Model

The import role gas pressure has played in modeling the air conditioning unit is stated in previous sections. Thus, the gas pressure model is develop based on theoretical calculation and measurement data.

The gas pressure model is represented by [13]:

$$\frac{dp_i}{dt}\frac{1}{p_i} = \frac{dm_i}{dt}\frac{1}{m_i} + \frac{dT_i}{dt}\frac{1}{T_i} \tag{2.3}$$

where p presents pressure, m is mass and T is the temperature. The temperature T is constant for this case. The gas pressure is mostly related to the gas mass in the chamber. The mass change is due to the compressor itself and the rate of mass change is directly related to the rotor speed. Thus, the gas pressure model is developed as

$$\frac{dp_{gas}}{dt} = (K\omega - p_{air})/\tau \tag{2.4}$$

The K is the constant relating gas pressure and speed, while the τ is the time constant of the gas pressure dynamics.

Since the load torque of the compressor is related to speed and the load torque of the gas pressure does the same, the load torque model is combined as

$$T_{load} = T_{load\_rated}(K_{\omega}\frac{\omega_r}{\omega_{r\_rated}} - K_p\frac{p_{gas}}{p_{gas\_rated}}) \quad (2.5)$$

Fig. 2.5 and Fig. 2.6 show the simulation result of gas pressure model compared with the measurement data.

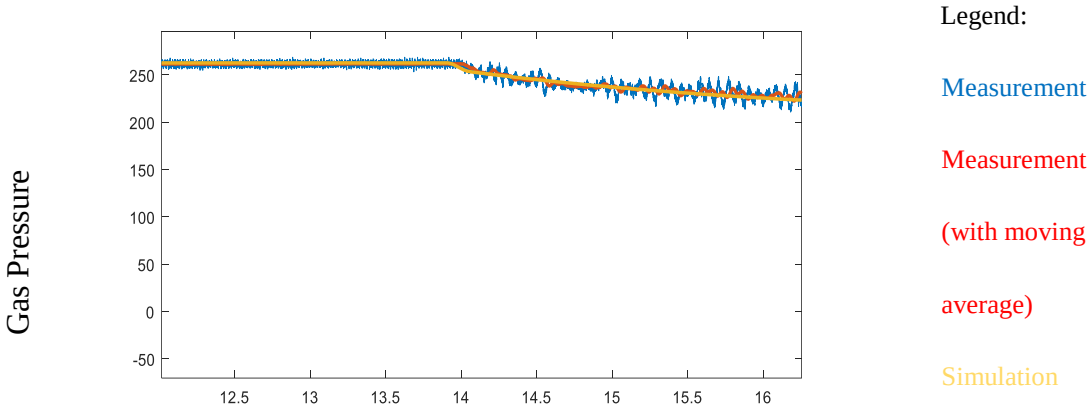


Fig 2.5 Simulation result of gas pressure model compared with the measurement data (stall)

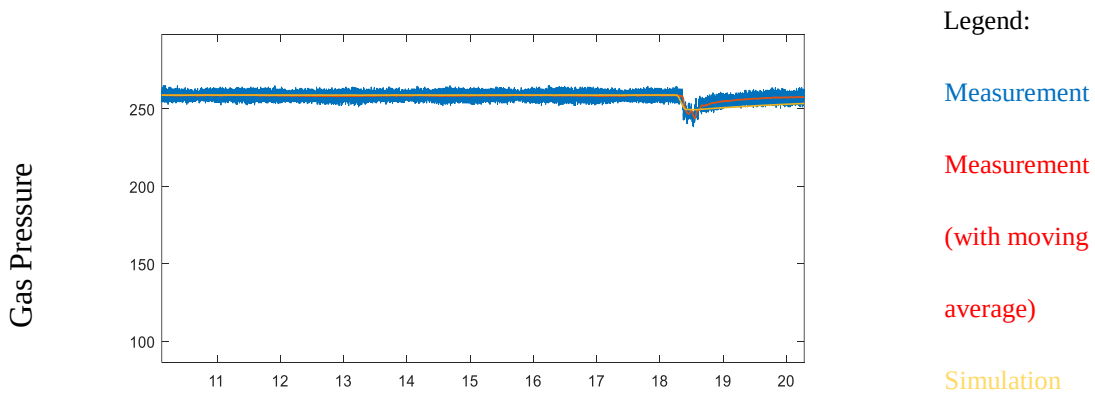


Fig 2.6 Simulation result of gas pressure model compared with the measurement data (no stall)

## 2.4 Dynamic Phasor Voltage Angle Compensation

The test data shows that the motor has different stall behavior when the fault occurs at different points on the voltage cycle. The voltage fault occurring when the voltage is at a zero crossing is more likely to cause the motor to stall than the fault at the voltage peak. This is confirmed from the point on wave model in Fig 2.4 and Fig. 2.5.

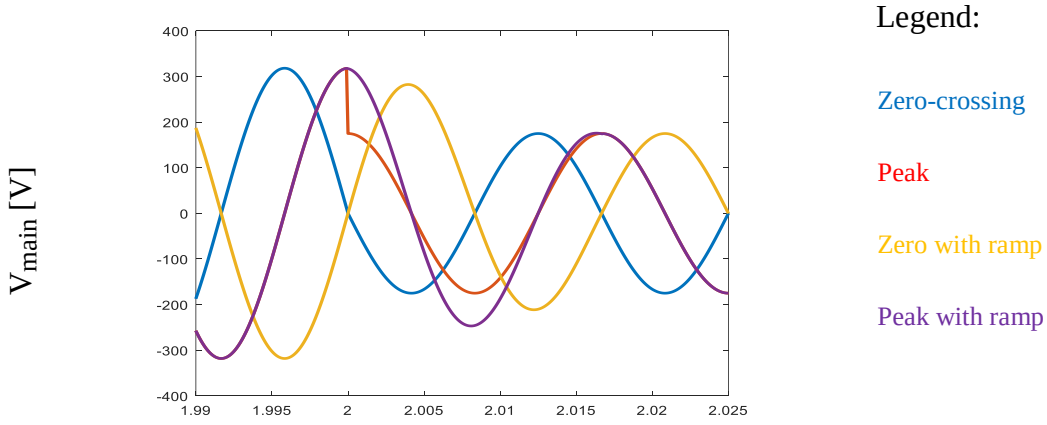


Fig. 2.4 Point on Wave simulation of different voltage fault points

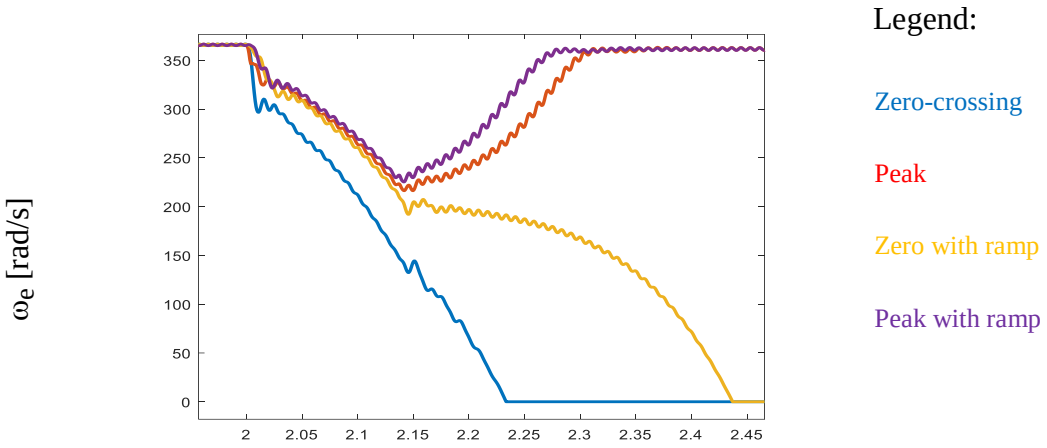


Fig. 2.5 Point on Wave simulation of different operating points

As shown in Fig 2.5, the fault at zero-crossing causes a stall while the fault at peak does not.

The point on wave model is able to capture the relationship between stalling and fault points. However, the dynamic phasor is a slower model that focuses on the amplitude of the signal, so some extra modeling is needed to allow the dynamic phasor to be able to capture the fault point difference. To study this difference, we compute a dynamic phasor model input by applying (1.43) to the voltage waveform. In Fig. 2.6 – Fig. 2.8 we show the fundamental frequency phase distortion that is apparent during the transient of the different fault locations.

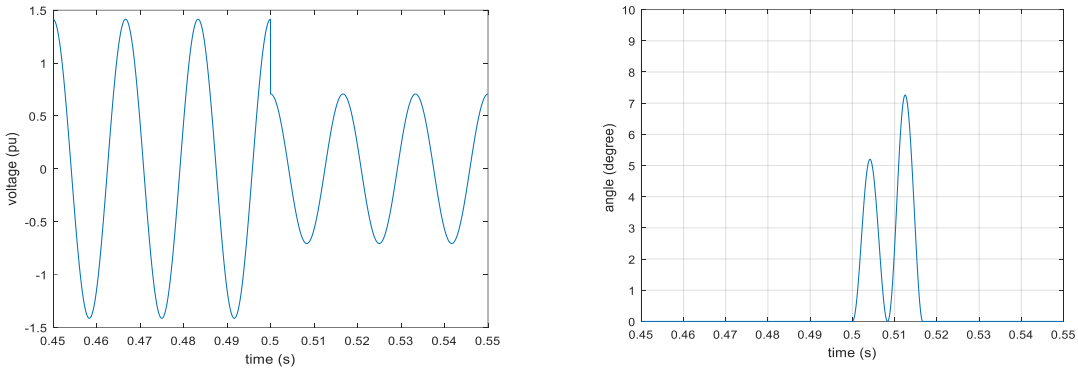


Fig 2.6 The angle distortion of the voltage fault on voltage phasor (peak)

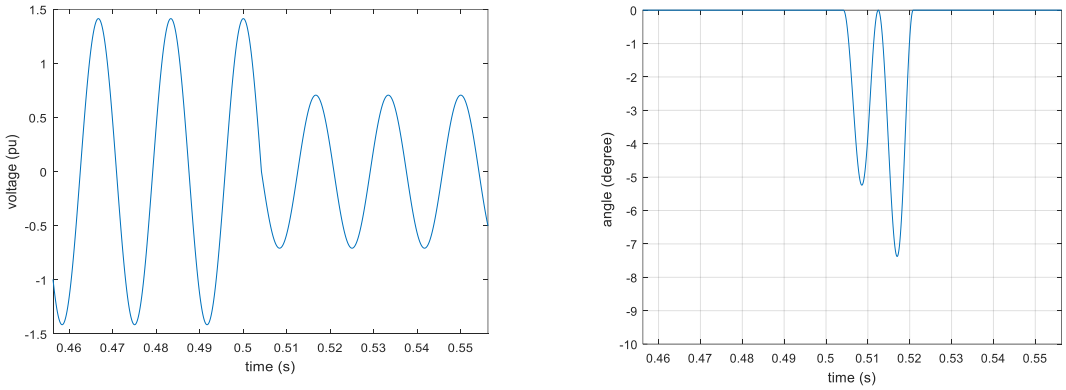


Fig 2.7 The angle distortion of the voltage fault on voltage phasor (zero-crossing)

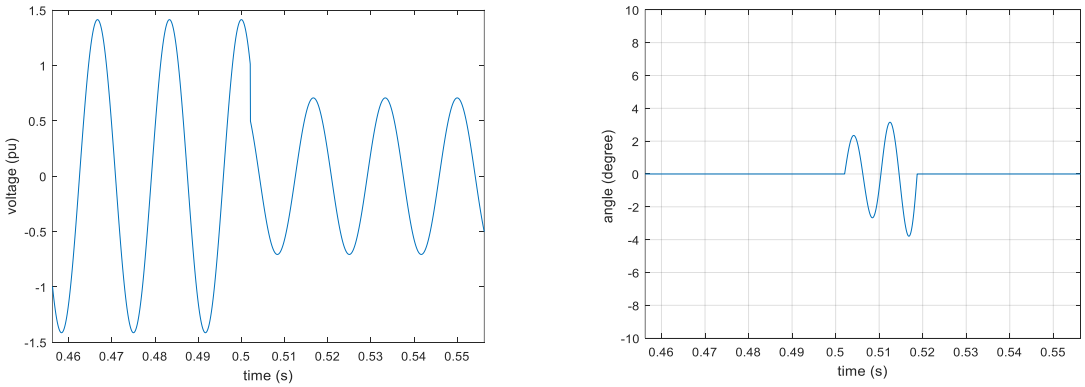


Fig 2.8 The angle distortion of the voltage fault on voltage phasor (45-degree)

From Fig 2.6 – Fig. 2.8, the fault at different points on waveform would cause different phase distortions of the voltage phasor. When the fault occurs at a zero crossing a negative angle is seen in the voltage phasor, while the peak introduces a positive angle and 45-degree would cause an average phase distortion around zero. So, an angle compensation is injected to the dynamic phasor model. Fig 2.7 shows the angle distortion for different fault levels occurring at different operating points.

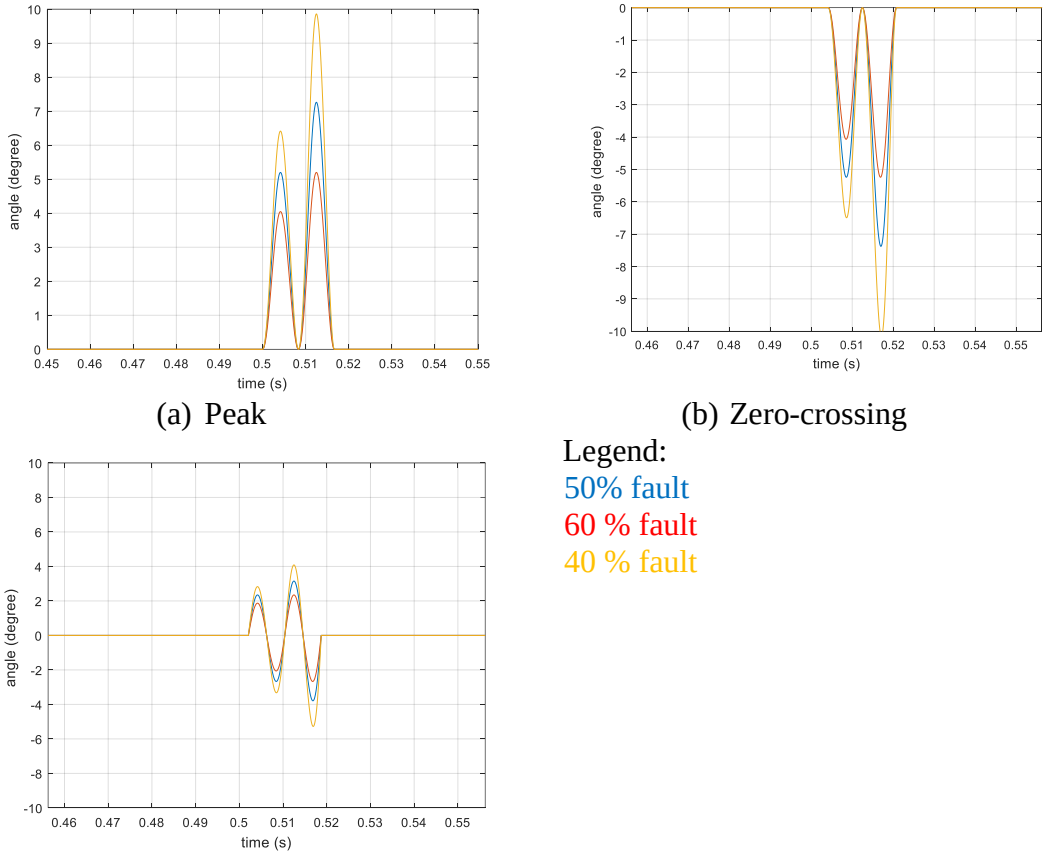


(a) Peak (b) Zero-crossing

(c) 45 degree

Fig. 2.7 Angle Plots for Different Fault Levels and Positions(a) peak (b) zero-crossing (c) 45-degree

As shown in Fig 2.7, the angle distortion increase as the fault percentage decreases. And the angle appears to have a square, rather than linear, relation to the fault level. Thus, the angle injection model is developed (2.6)

$$\theta_{injected} = \frac{\theta_{constant}}{(fault\ level)^2} \tag{2.6}$$

where, the $\theta_{constant}$ is the constant for the fault point. For the same fault point, the $\theta_{constant}$ is same. For different fault points, $\theta_{constant}$ varies. $\theta_{constant} = 0$ for fault at peak; $\theta_{constant}$ is negative for fault at zero-crossing. $\theta_{constant\ \ zero-crossing} < \theta_{constant\ \ 45-degree} < 0$.

## 2.5 Ramp Fault

Also, voltage fault with ramp is tested. The voltage fault with ramp means that the voltage reaches fault level in one cycle period instead of instantaneously. When the voltage has a ramp voltage, the motor is more likely to stall at a peak fault and less likely to stall at a zero-crossing fault, compared with voltage fault without ramp. Fig. 2.8 shows the voltage waveform and angle distortion of a ramp fault at peak.

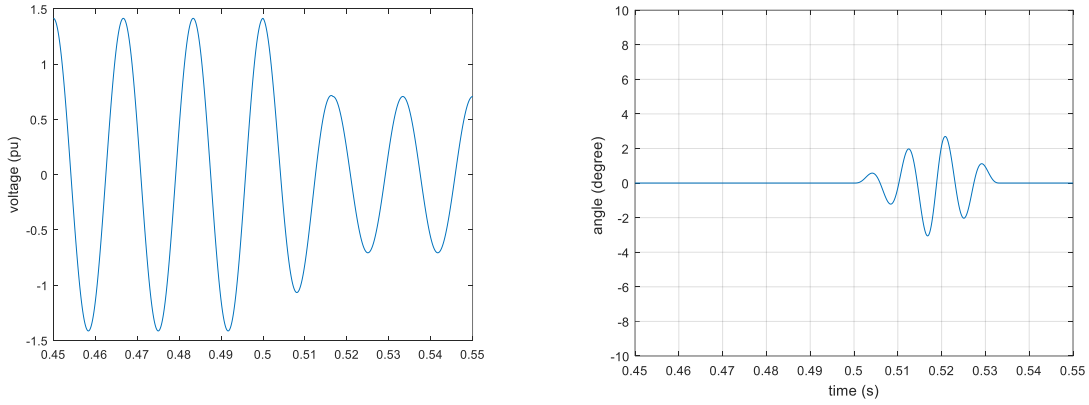


Fig 2.7 The angle distortion of the voltage fault on voltage phasor with ramp fault at peak

The average phase distortion of the ramp fault is around zero. The phase distortion of the ramp fault at different location and different level is studied, and the result is shown in Fig. 2.9 and Fig. 2.10.

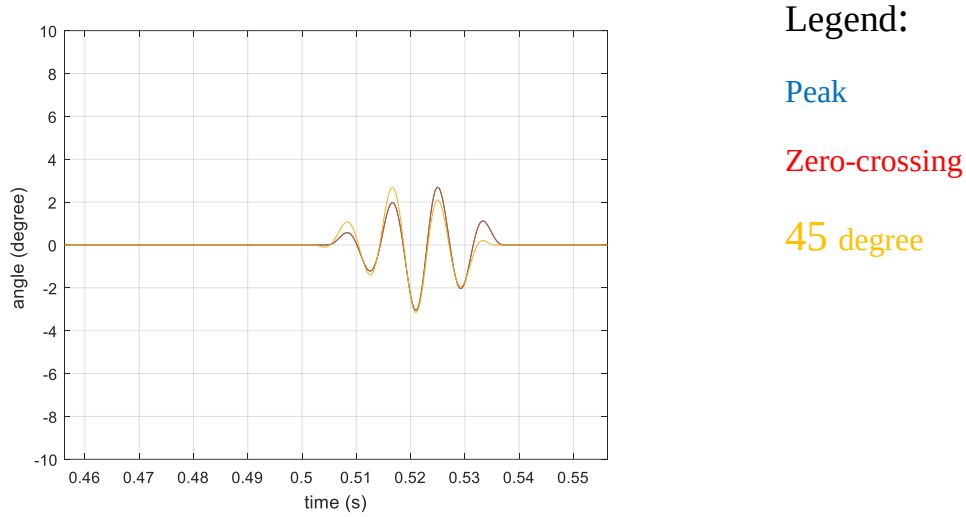


Fig. 2.9 Ramp Fault Angle Plots for Different Positions

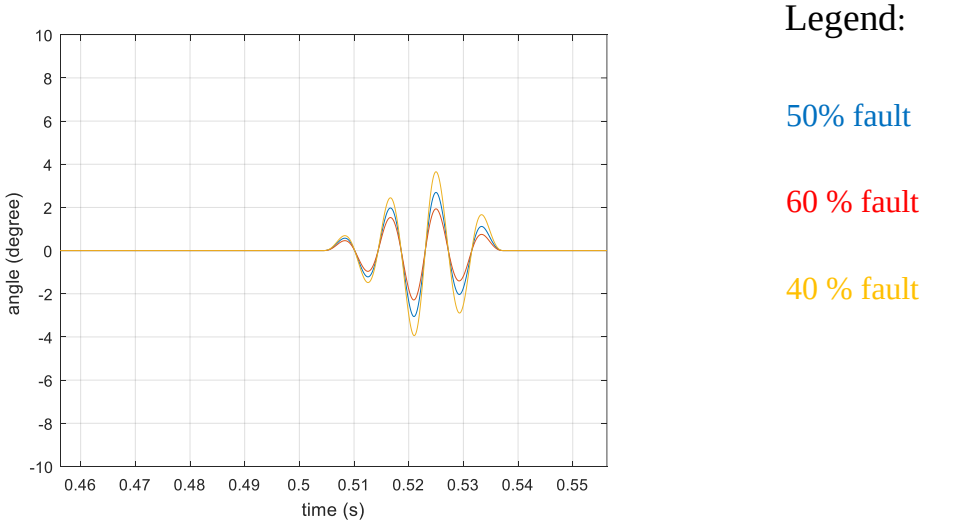


Fig. 2.10 Ramp Fault Angle Plots for Different Fault Levels

As shown in Fig. 2.9, the phase distortions for different fault positions are all close to zero for ramp fault. Thus, the angle injection for ramp fault is assumed to be same as 45-degree. At different fault levels, the phase distortion of ramp fault has same pattern as that of non-ramp fault, so the same angle model is applied to the ramp fault.

## 2.6 Summary

This chapter introduced the additional model for the motor modeling. Firstly, the load torque for different compressor is studied. Then the gas pressure model is analyzed and developed to establish a model for load torque and moment of inertia. Also, the angle injection technique is introduced to make the dynamic phasor model consistent with measurement.

# Chapter 3 *Parameter Estimation Model*

The previous sections discussed about the models for motor modeling. In this chapter a parameter estimation model is implemented to match the simulation results with measurement data.

## 3.1 Least Square Model

AC units have been tested in the lab and the parameters of the motor are estimated to fit the simulation results to measured data.

In fitting a function $\hat{y}(t;p)$ of an independent variable t and a vector of n parameters p to a set of m data points $(t_i, y_i)$, it is convenient to minimize the sum of the weighted squares of the errors between the measured data $y\ (t_i)$ and the curve-fit function $\hat{y}(t_i;p)$. This is the least squares method. [14]

$$x^2(p) = \sum_{i=1}^{m} \left[ \frac{y\ (t_i) - \hat{y}\ (t_i;p)}{\sigma_{yi}} \right]^2 \tag{3.1}$$

$$= (y - \hat{y}(p))^T \mathbf{W} (y - \hat{y}(p)) \tag{3.2}$$

$$= y^T \mathbf{W} y - y^T \mathbf{W} \hat{y} + \hat{y}^T \mathbf{W} \hat{y} \tag{3.3}$$

where $\sigma_{yi}$ is the measurement error for measurement $y(t_i)$. W is the weighting function.

The Gauss-Newton method is one of the least square methods that presumes the objective function is approximately near the optimal solution. [15] [16]

The function can be approximated through a first-order Taylor series expansion.

$$\hat{y}(p + \mathrm{h}) \approx \hat{y}(p) + \left[\frac{\partial \hat{y}}{\partial p}\right]\mathrm{h} = \hat{y} + \mathbf{J}\mathrm{h} \tag{3.4}$$

$$x^2(p + \mathrm{h}) = y^T\mathbf{W}y + \hat{y}^T\mathbf{W}\hat{y} - 2y^T\mathbf{W}\hat{y} - 2(y - \hat{y})^T\mathbf{W}\mathbf{J}\mathrm{h} + \mathrm{h}^T\mathbf{J}^T\mathbf{W}\mathbf{J}\mathrm{h} \tag{3.5}$$

The jacobian matrix is $\mathbf{J} = [\partial\hat{y}/\partial\mathrm{p}]$, and the goal is to minimize $x^2$ so that $\partial x^2/\partial h = 0$.

$$\frac{\partial}{\partial \mathrm{h}}x^2(p + \mathrm{h}) \approx -2(y - \hat{y})^T\mathbf{W}\mathbf{J} + 2\mathrm{h}^T\mathbf{J}^T\mathbf{W}\mathbf{J} \tag{3.6}$$

$$[\mathbf{J}^T\mathbf{W}\mathbf{J}]\mathrm{h} = \mathbf{J}^T\mathbf{W}(y - \hat{y})^T \tag{3.7}$$

The Levenberg-Marquardt algorithm updates parameters in (3.8)

$$[\mathbf{J}^T\mathbf{W}\mathbf{J} + \lambda\mathbf{I}]\mathrm{h} = \mathbf{J}^T\mathbf{W}(y - \hat{y})^T \tag{3.8}$$

When the estimation is close to the optimal condition, the λ value is small and the algorithm updates parameters like the Gauss-Newton method. When the estimation is

far from the optimal values. Generally, λ starts with a large value assuming the initial guess is far from the optimal condition [16] [17] [18]. If the iteration results in a better solution, λ is decreased, otherwise λ is increased.

## 3.2 Parameter Estimation Starting Point

As mentioned in previous section, the choice of a starting point is critical in parameters estimation. Choosing a good starting point can save lots of computational time and typically would result in a better estimation.

Since the stator resistance is the only parameter that can be directly measured and the stator terminal voltage and current are the only machine variables that can be measured, certain techniques for choosing the starting point is needed.

The resistance of the machine winding can be achieved by the measurement data while the motor is stalled. While the motor is stalling the reactance is small and the $\frac{R_r}{s}$ term becomes $R_r$, so that the initial guess of the stator, rotor resistance and stator, rotor leakage reactance can be found as show in Fig 3.1

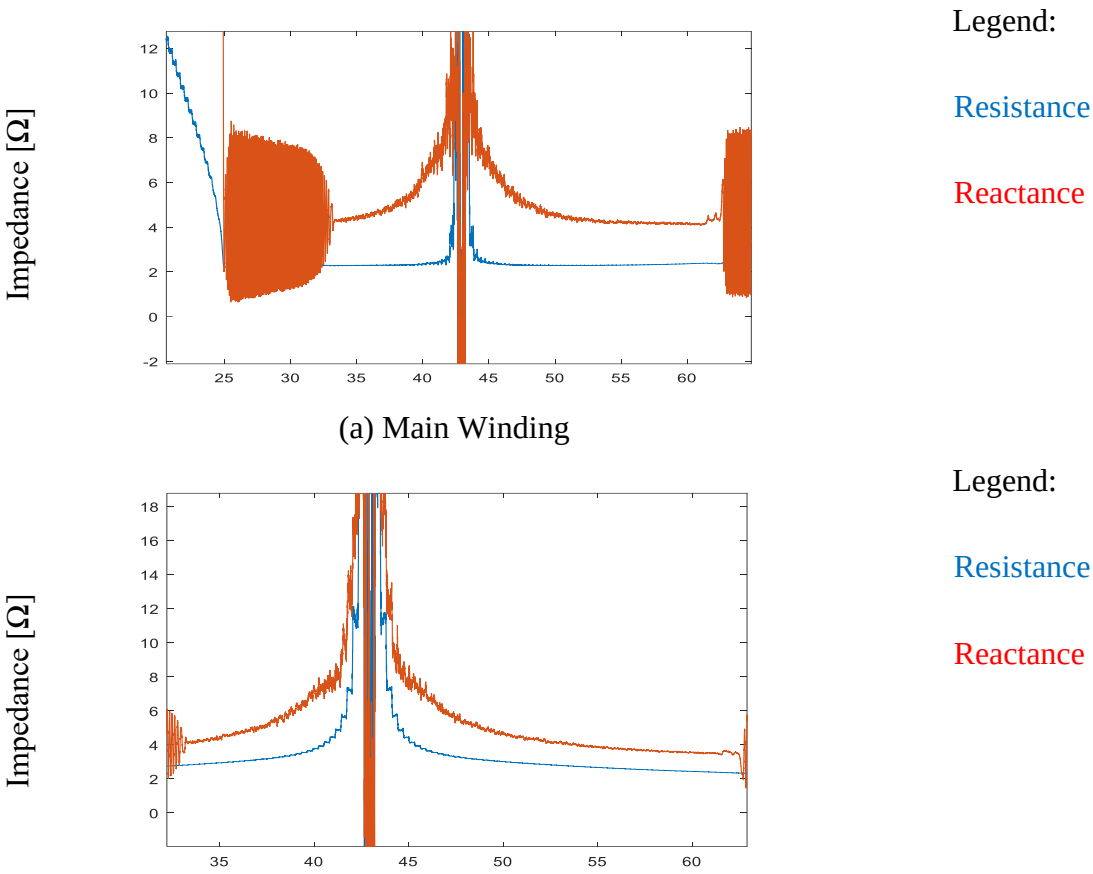


(a) Main Winding

(b) Auxiliary Winding

Fig. 3.1 Main and Auxiliary Winding Impedance at zero speed (a) Main Winding (b) Auxiliary Winding

Apart from the resistance and leakage inductance, the magnetizing inductance and slip frequency are also important parameters to estimate. The initial starting value can be estimated as (3.9-3.10) [19]

$$P \approx \frac{V_s^2}{\frac{R_r}{s}} \tag{3.9}$$

$$Q \approx \frac{V_s^2}{X_m} \tag{3.10}$$

Fig 3.2 shows the measured data for calculated initial starting value of $X_m$and $\frac{R_r}{s}$ at steady state.

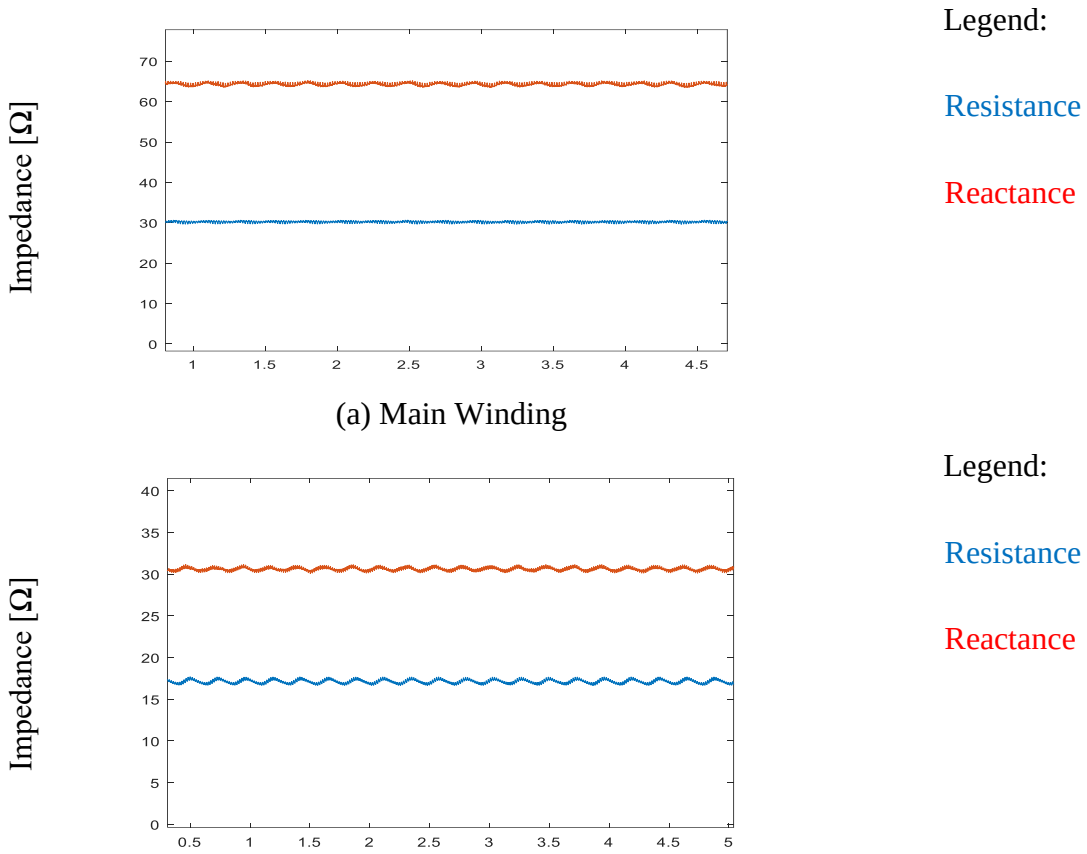


(a) Main Winding

(b) Auxiliary Winding

Fig. 3.2 Main and Auxiliary Winding Impedance at steady state (a) Main Winding (b) Auxiliary Winding

## 3.3 Effect of Parameter Estimation

Fig 3.3 and Fig. 3.4 shows the simulation result with initial guess of the parameters for the reciprocating compressor.

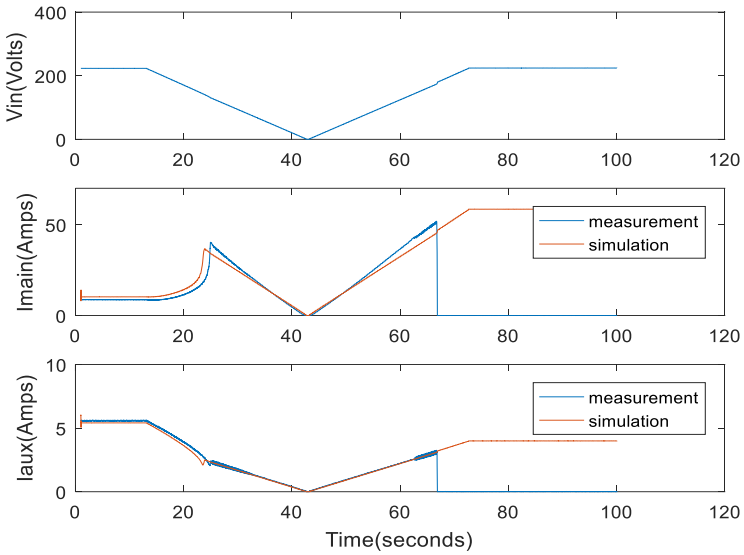


Fig 3.3 Voltage Ramp Test Current plots with initial guess parameters (reciprocating compressor)

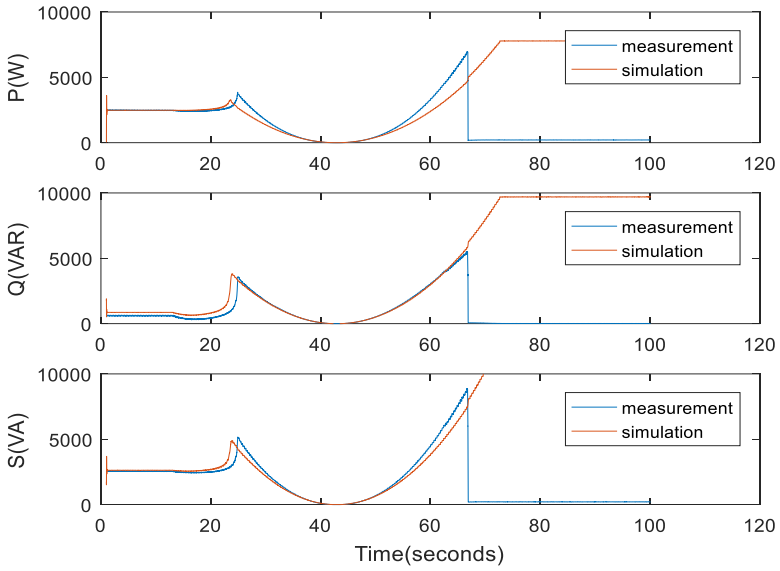


Fig 3.4 Voltage Ramp Test Power plots with initial guess parameters (reciprocating compressor)

The initial guess is already close to the measure data, which means that the estimation can converge faster and more accurate. The effect of the parameter estimation is shown in Fig 3.5 and Fig. 3.6.

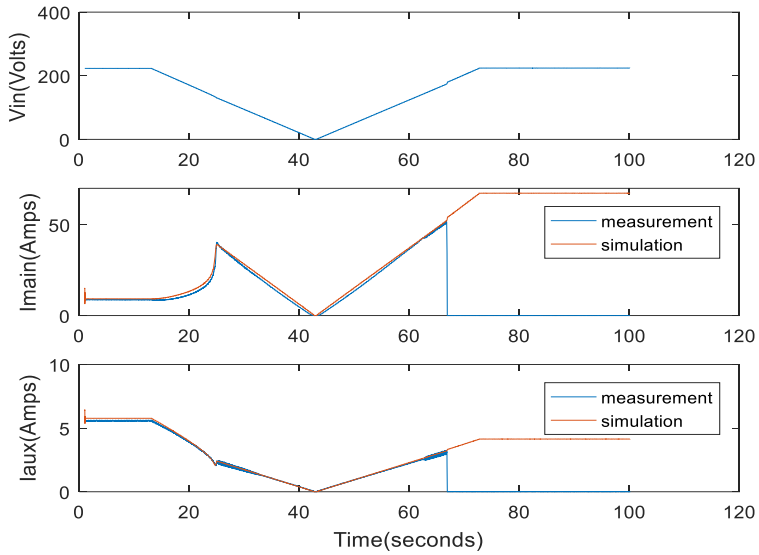


Fig 3.5 Voltage Ramp Test Current plots with final estimated parameters (reciprocating compressor)

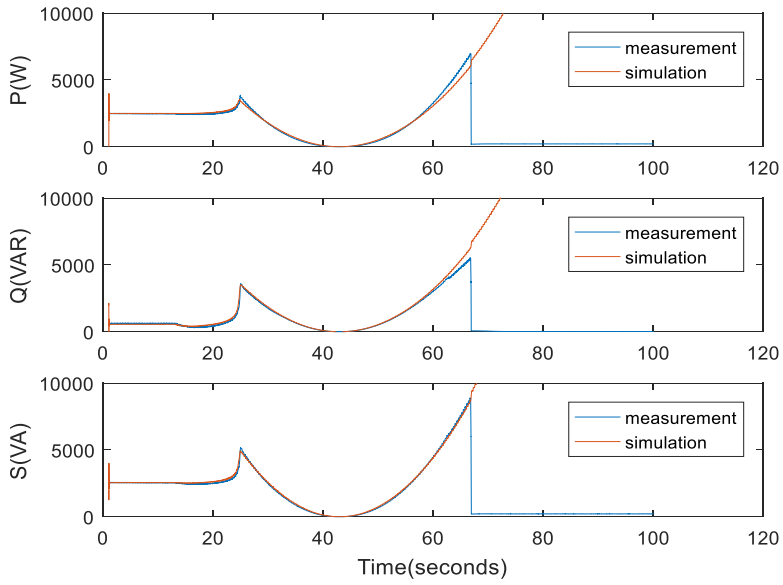


Fig 3.6 Voltage Ramp Test Power plots with final estimated parameters (reciprocating compressor)

Since the initial guess is close to the measured value, the result of parameter estimation is good for the reciprocating compressor. Table 3.1 shows the parameters before and after the estimation.

Table 3.1 Parameters Used before and after the Estimation (reciprocating compressor)

| Parameters | Initial Guess | Final Match |
|---|---|---|
| Main Winding Magnetizing Inductance (Lms) [mH] | 104.85 | 109.52 |
| Auxiliary Winding Magnetizing Inductance (LmS) [mH] | 138.89 | 144.84 |
| Rotor Leakage Inductance (Llr) [mH] | 3.475 | 3.28 |
| Main Winding Stator Leakage Inductance (Lls) [mH] | 4.768 | 2.54 |
| Auxiliary Winding Stator Leakage Inductance (LlS) [mH] | 3.214 | 2.23 |
| Rotor Resistance (Rr) [Ω] | 1.129 | 1.04 |

Then the parameter estimation of scroll compressor is studied. Fig 3.7 and Fig. 3.8 show the simulation results with initial guess parameters. Fig. 3.9 and Fig 3.10 show the results after estimation.

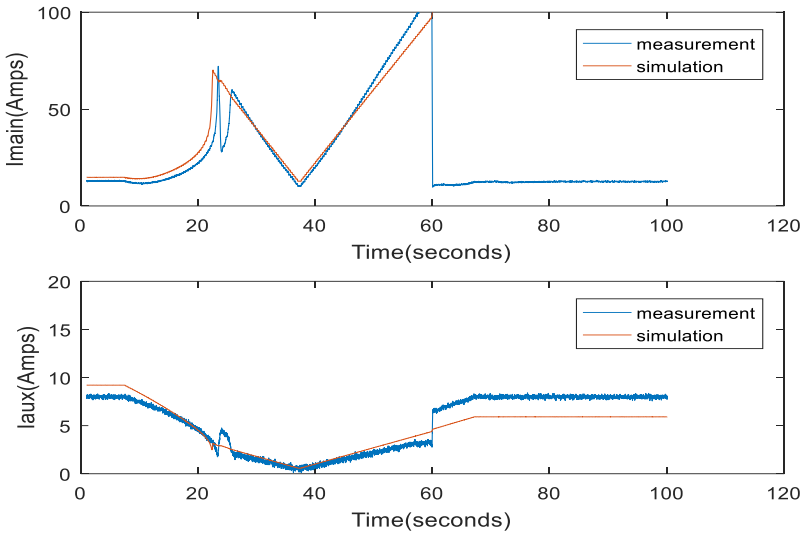


Fig 3.7 Voltage Ramp Test Current plots with initial guess parameters (scroll compressor)

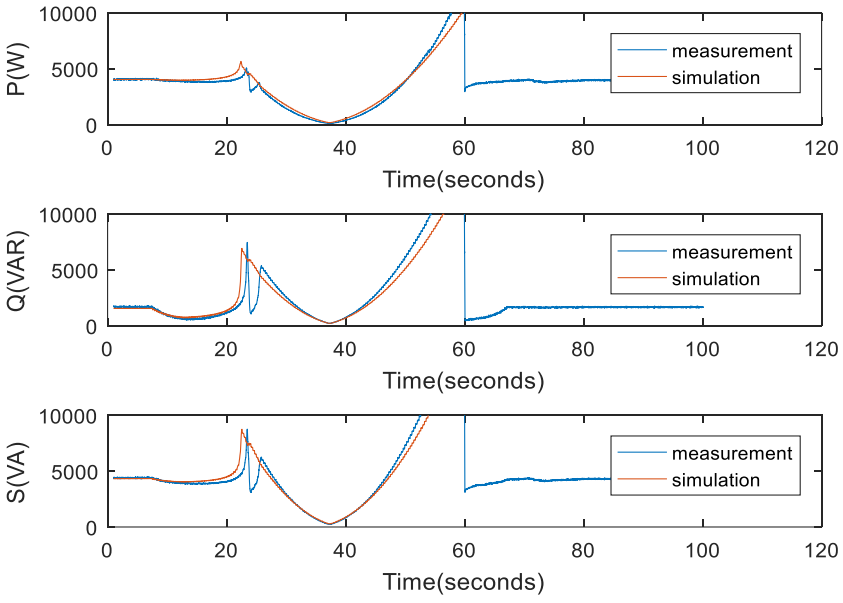


Fig 3.8 Voltage Ramp Test Power plots with initial guess parameters (scroll compressor)

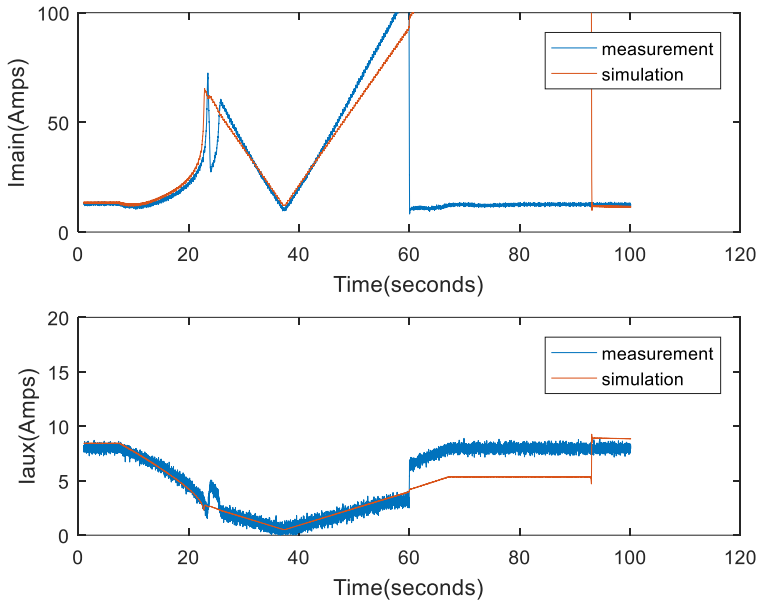


Fig 3.9 Voltage Ramp Test Current plots with final estimated parameters (scroll compressor)

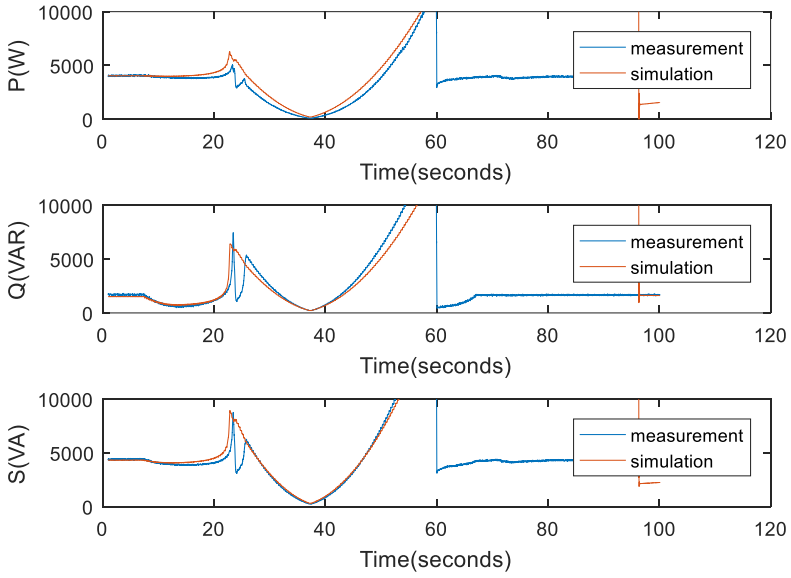


Fig 3.10 Voltage Ramp Test Current plots with final estimated parameters (scroll compressor)

The parameters are listed in Table 3.2. The parameter method used focuses more on the electrical parameters. So that the transient caused by the mechanical system are not modeled well. This phenomenon is more obvious for the scroll compressor case.

Table 3.2 Parameters Used before and after the Estimation (scroll compressor)

| Parameters | Initial Guess | Final Match |
|---|---|---|
| Main Winding Magnetizing Inductance (Lms) [mH] | 63.66 | 67.93 |
| Auxiliary Winding Magnetizing Inductance (LmS) [mH] | 114.99 | 123.81 |
| Rotor Leakage Inductance (Llr) [mH] | 1.326 | 1.351 |
| Main Winding Stator Leakage Inductance (Lls) [mH] | 2.652 | 2.0734 |
| Auxiliary Winding Stator Leakage Inductance (LlS) [mH] | 1.365 | 3.110 |
| Rotor Resistance (Rr) [Ω] | 0.5 | 0.533 |

## 3.4 Summary

This chapter discussed the parameter estimation model. It consists of the least square model to update the parameters and the technique to choose the starting point. The effect of the parameter estimation is shown for the two compressors.

# Chapter 4 *Simulation Results and Model Validation*

This chapter presents the comparison between simulation results and measurement data for steady state tests, voltage ramp test and stall behavior tests.

## 4.1 Steady State Tests

The steady state behavior of the motor is important to estimate the electrical parameters. Fig. 4.1 and Fig. 4.2 shows the power and current for the motor with reciprocating compressor as load when voltage fault lasts for 5 cycles at 55 percent. And then the voltage recover to 85 percent of the nominal voltage after the fault with point on wave model.

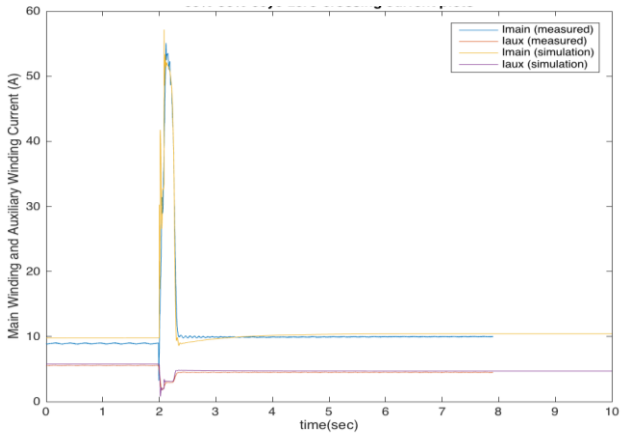


Fig 4.1 Steady State Current plots with 55 percent fault lasts 5 cycles with Point on Wave model (reciprocating compressor)

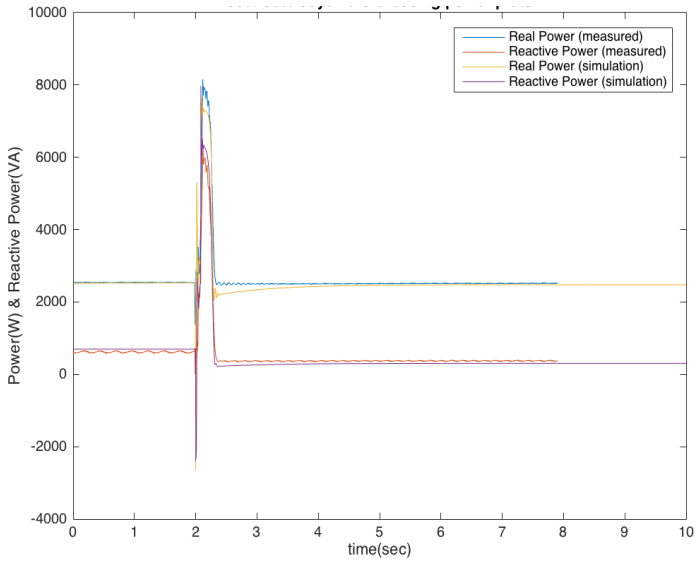


Fig 4.2 Steady State Power plots with 55 percent fault lasts 5 cycles with Point on Wave model (reciprocating compressor)

The simulation result and measurement data are transformed into synchronous reference frame for better observation. Since the AC waveforms of the machine will be "DC" at synchronous reference frame.

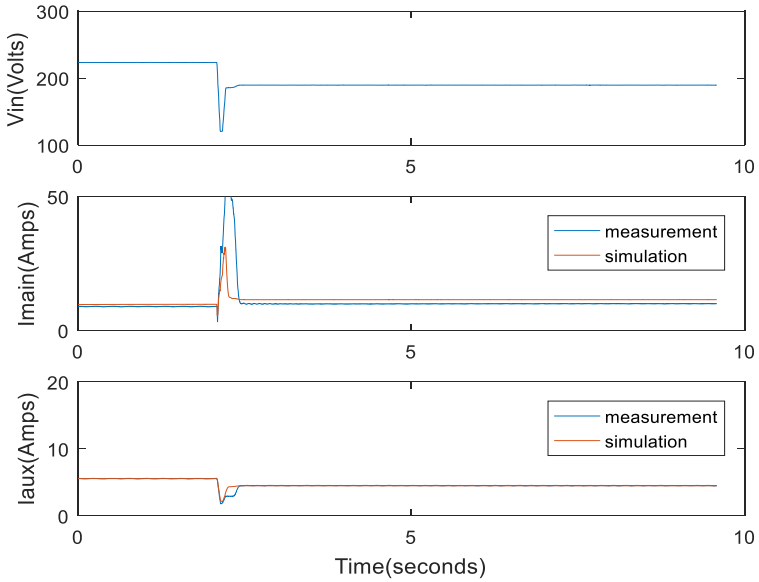


Fig 4.3 Steady State Current plots with 55 percent fault lasts 5 cycles with Dynamic Phasor model (reciprocating compressor)

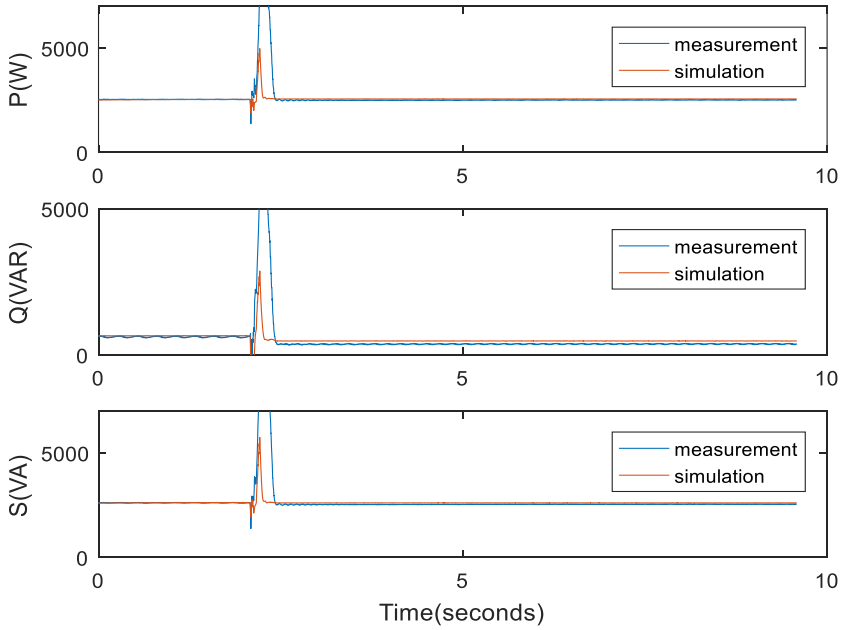


Fig 4.4 Steady State Power plots with 55 percent fault lasts 5 cycles with Dynamic Phasor model (reciprocating compressor)

Fig. 4.3 and Fig. 4.4 shows the simulation result with same case as Fig. 4.1 and Fig. 4.2 with dynamic phasor model. As expected, the dynamic phasor model cannot capture the transient response as well as the point on wave model. However, the steady state estimation of the dynamic phasor is good enough.

As shown in the plots, the motor keeps going after a voltage fault of 55% and 5 cycles. Then voltage fault of 55% and 6 cycles is test and the result is shown in Fig 4.5 to Fig 4.8. Both point on wave and dynamic phasor model are shown.

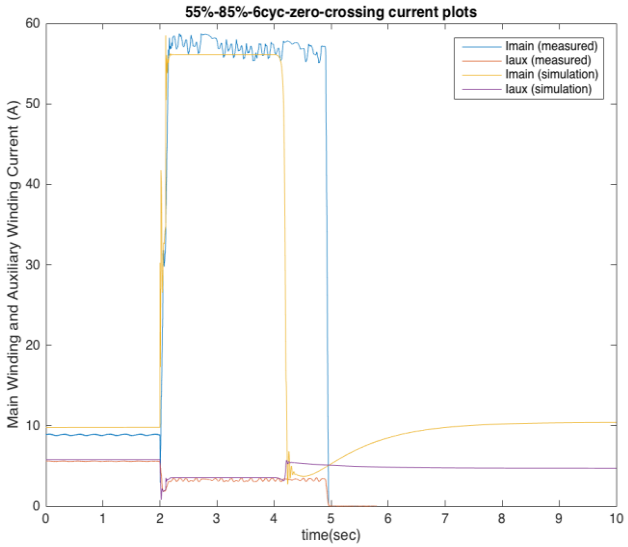


Fig 4.5 Steady State Current plots with 55 percent fault lasts 6 cycles with Point on Wave model (reciprocating compressor)

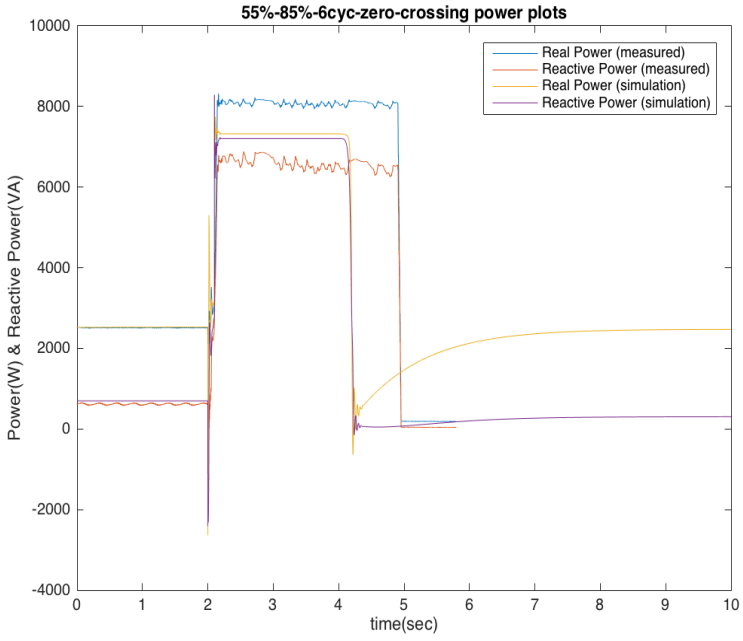


Fig 4.6 Steady State Power plots with 55 percent fault lasts 6 cycles with Point on Wave model (reciprocating compressor)

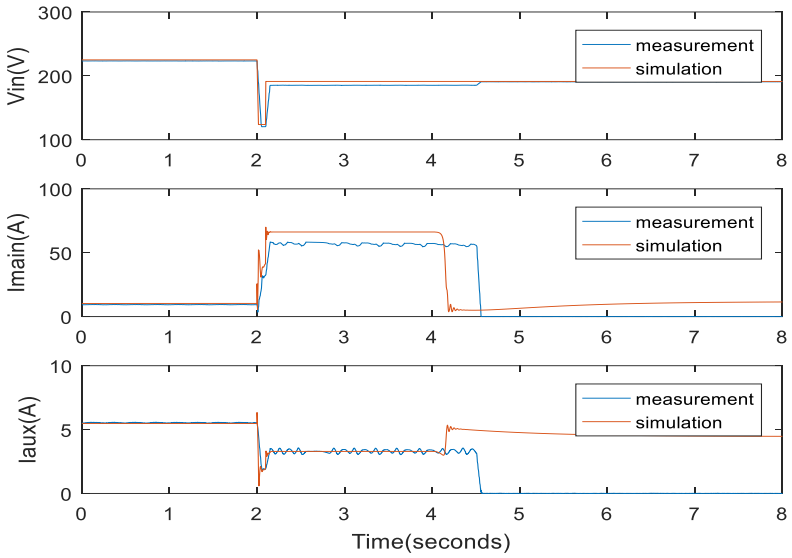


Fig 4.7 Steady State Current plots with 55 percent fault lasts 6 cycles with Dynamic Phasor model (reciprocating compressor)

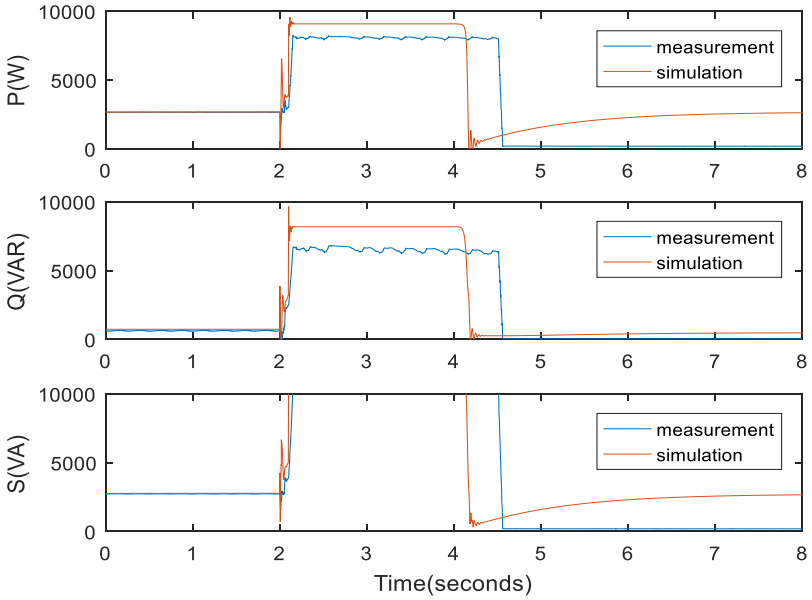


Fig 4.8 Steady State Power plots with 55 percent fault lasts 6 cycles with Dynamic Phasor model (reciprocating compressor)

Previous plots show the simulation results for the motor with reciprocating compressor as load. The steady state behavior of the motor with scroll compressor load is presented in Fig. 4.9 to Fig. 4.12.

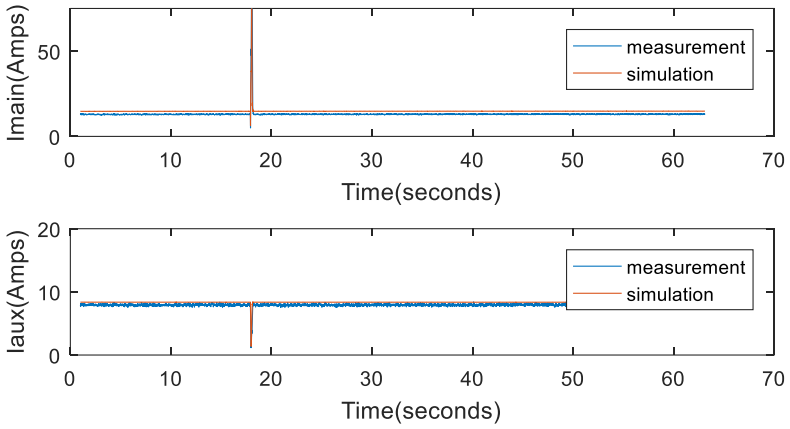


Fig 4.9 Steady State Current plots with 55 percent fault lasts 5 cycles with Dynamic Phasor model (scroll compressor)

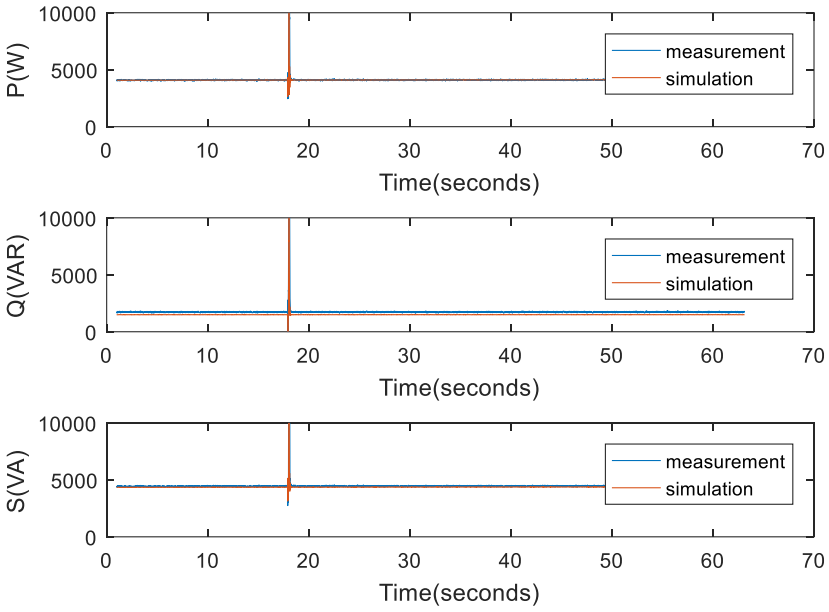


Fig 4.10 Steady State Power plots with 55 percent fault lasts 5 cycles with Dynamic Phasor model (scroll compressor)

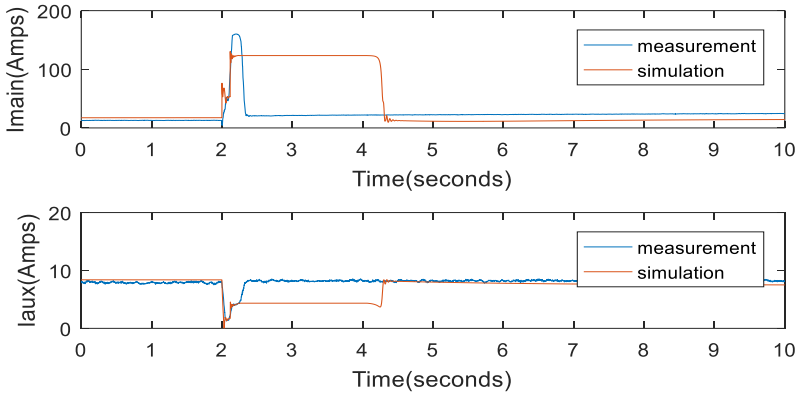


Fig 4.11 Steady State Current plots with 55 percent fault lasts 6 cycles with Dynamic Phasor model (scroll compressor)

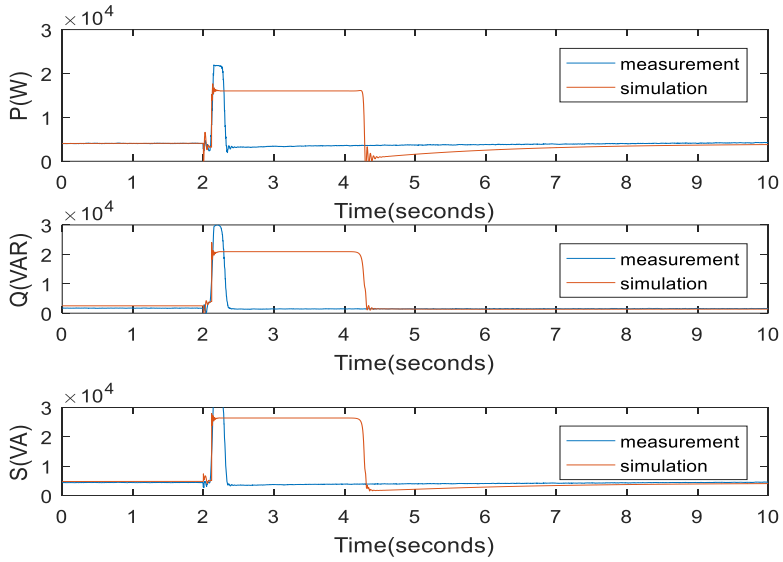


Fig 4.12 Steady State Power plots with 55 percent fault lasts 6 cycles with Dynamic Phasor model (scroll compressor)

The steady state result of the simulation matches the measure data as expected. However, the transient behavior of the motor does not match perfectly. So, extra parameter estimation of the mechanical parameters such as the torque coefficient, the moment of inertia and the saturation property is needed. The data for those estimations are not sufficient. Extra tests may be needed for the estimation of the mechanical parameters for future work.

## 4.2 Voltage Ramp Tests

A slow speed voltage ramp is used as the input voltage of the motor to test the motor behavior at different operation points. Fig. 4.13 and Fig. 4.14 shows the voltage ramp test for the reciprocating compressor with point on wave model. Same as previous section, results of point on wave model are transformed to synchronous frame “DC” representations.

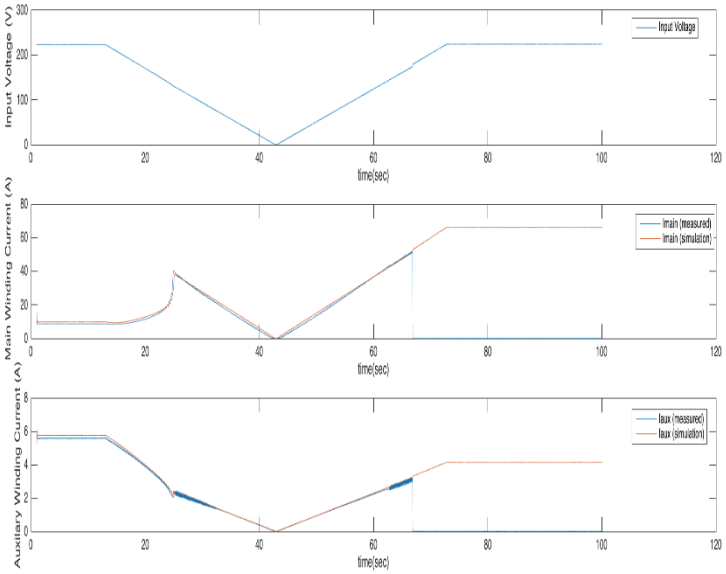


Fig 4.13 Voltage Ramp Test Current plots with Point on Wave model (reciprocating compressor)

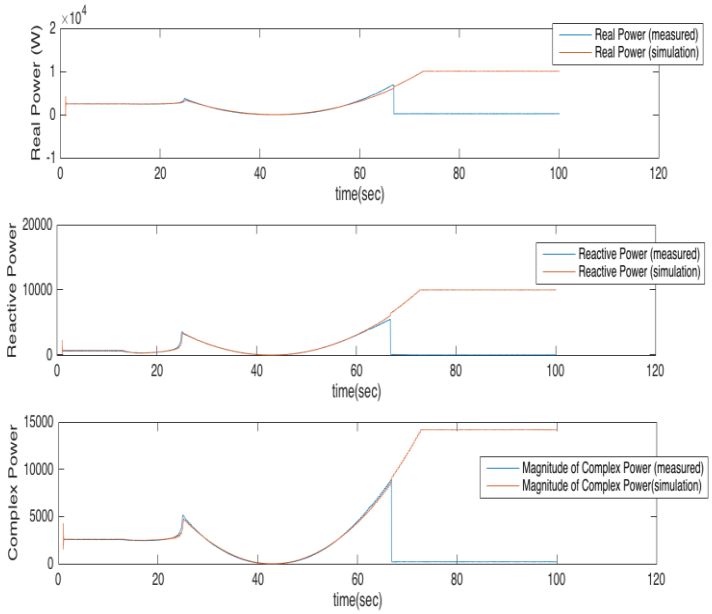


Fig 4.14 Voltage Ramp Test Power plots with Point on Wave model (reciprocating compressor)

As shown in the plots, the simulation results match the measurement well for the point on wave model. Then the results of dynamic phasor model are studied and shown in Fig. 4.15 and Fig. 4.16.

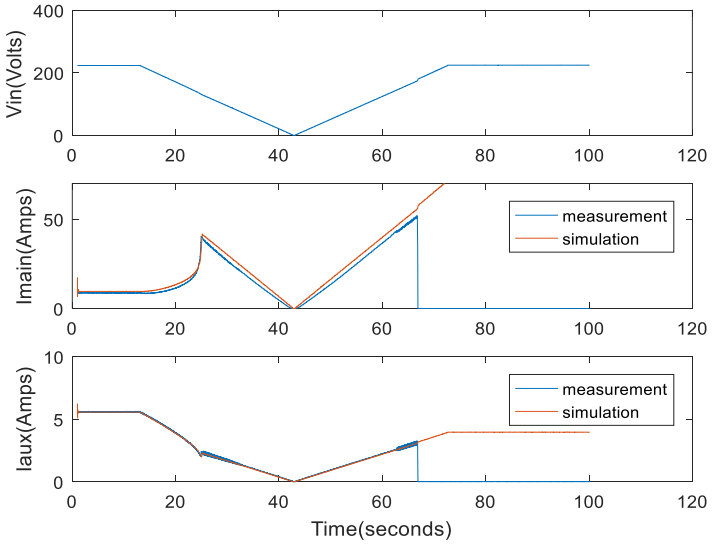


Fig 4.15 Voltage Ramp Test Current plots with Dynamic Phasor model (reciprocating compressor)

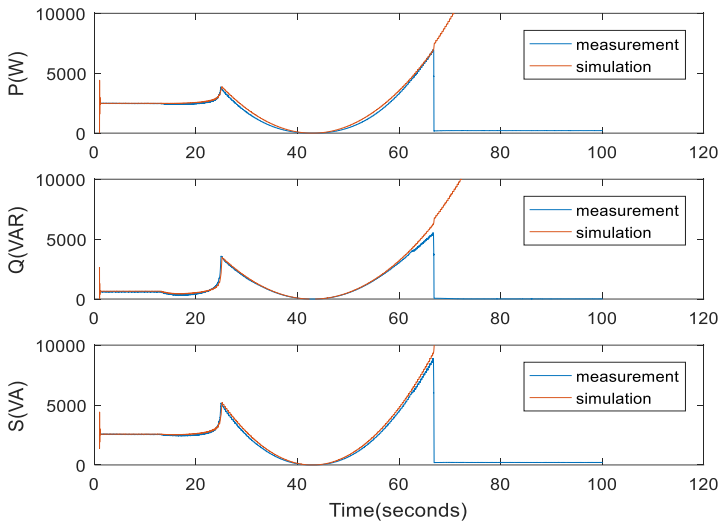


Fig 4.16 Voltage Ramp Test Power plots with Dynamic Phasor model (reciprocating compressor)

The result that the ramp test simulation result matches the measured data well. The reactive power drop due to saturation is also modeled. After the ramp test the motor current goes to zero, the reason of this is not modeled here and may be modeled in the future work.

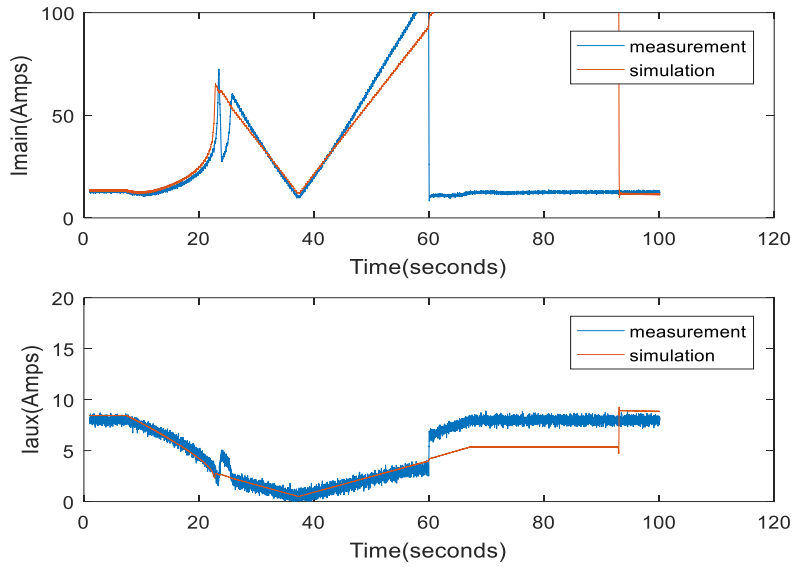


Fig 4.17 Voltage Ramp Test Current plots with final estimated parameters (scroll compressor)

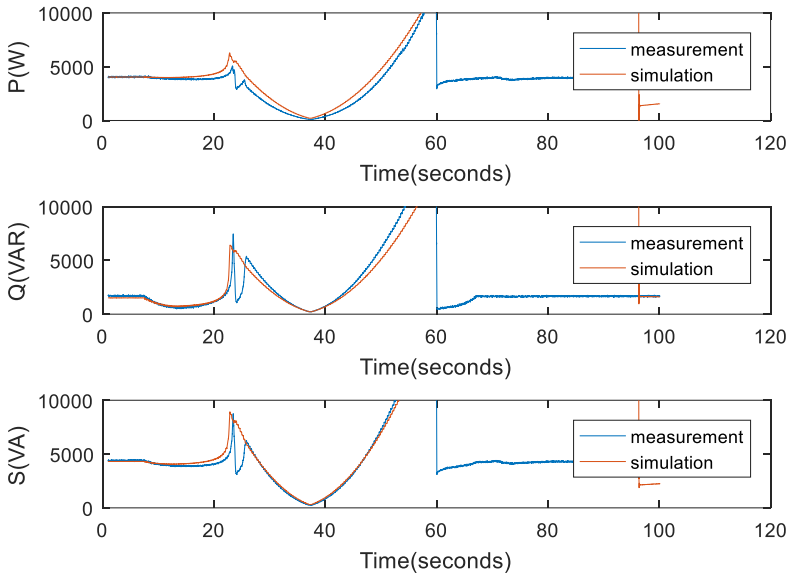


Fig 4.18 Voltage Ramp Test Power plots with final estimated parameters (scroll compressor)

Fig. 4.17 and Fig. 4.18 shows the ramp test for scroll compressor. The transient behavior of the scroll compressor is not modeled as good as the reciprocating compressor. The dynamics of the scroll compressor might not be fully modeled and can be improved in future work.

## 4.3 Stall Behavior Analysis

It is hard to get the exact model of the motor in transient response, due to physical constraints of the air conditioner unit. The most desired feature of the model is to be able to predict the stall behavior of the motor for FIDVR analysis. Thus, the stall behavior matching analysis is performed.

Table 4.1 to Table 4.4 show the stall behavior of the motor with reciprocating compressor. The mechanical parameters such as load torque and moment of inertia are tuned to match the stall behavior of the case where voltage fault occurs at peak with no ramp. Then the simulated stall behavior should match the test data for the remaining cases. Although the remaining cases do not match perfectly, in most of the cases they match well, and the rest of them are off by 1 or 2 cycles. This is acceptable without a perfect model of the mechanical system.

| Table 4.1 Voltage Fault at Peak with no ramp (reciprocating compressor) | | |
|---|---|---|
| Voltage Fault | Measured Stall Duration (cycles) | Simulation Stall Duration (cycles) |
| 30% | 3 | 3 |
| 35% | N/A | 4 |
| 40% | 5 | 5 |
| 45% | N/A | 6 |
| 50% | 7 | 7 |
| 55% | N/A | 10 |

| Table 4.2 Voltage Fault at zero crossing with no ramp (reciprocating compressor) | | |
|---|---|---|
| Voltage Fault | Measured Stall Duration (cycles) | Simulation Stall Duration (cycles) |
| 30% | N/A | N/A |
| 35% | N/A | N/A |
| 40% | N/A | N/A |
| 45% | N/A | 3 |
| 50% | 3 | 4 |
| 55% | 6 | 6 |
| 60 | 10 | 10 |

| Table 4.3 Voltage Fault at Peak with ramp (reciprocating compressor) | | |
|---|---|---|
| Voltage Fault | Measured Stall Duration (cycles) | Simulation Stall Duration (cycles) |
| 30% | N/A | N/A |
| 35% | N/A | N/A |
| 40% | 4 | 3 |
| 45% | N/A | 4 |
| 50% | 5 | 6 |
| 55% | 7 | 9 |

| Table 4.4 Voltage Fault at zero crossing with ramp (reciprocating compressor) | | |
|---|---|---|
| Voltage Fault | Measured Stall Duration (cycles) | Simulation Stall Duration (cycles) |
| 30% | N/A | N/A |
| 35% | N/A | N/A |
| 40% | N/A | 3 |
| 45% | 5 | 4 |
| 50% | 6 | 6 |
| 55% | 8 | 9 |
| 60 | 10 | 11 |

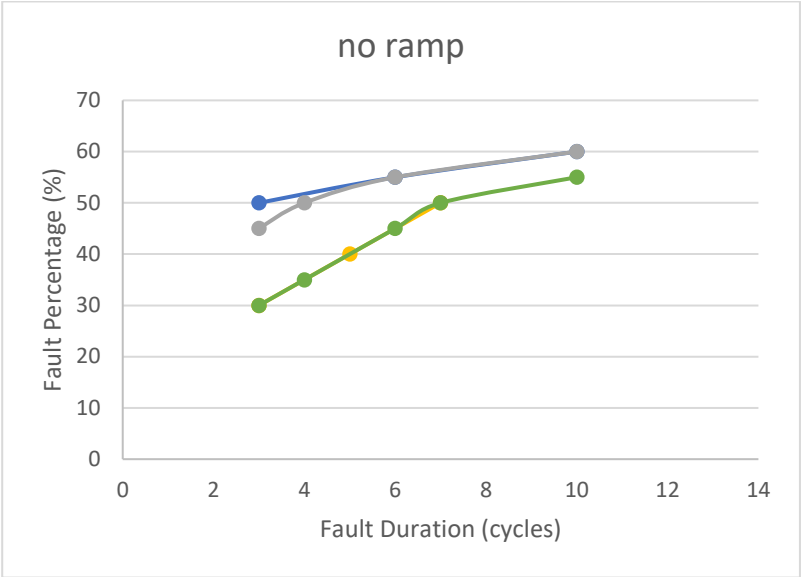


Fig 4.19 Stall analysis for reciprocating compressor with no voltage ramp

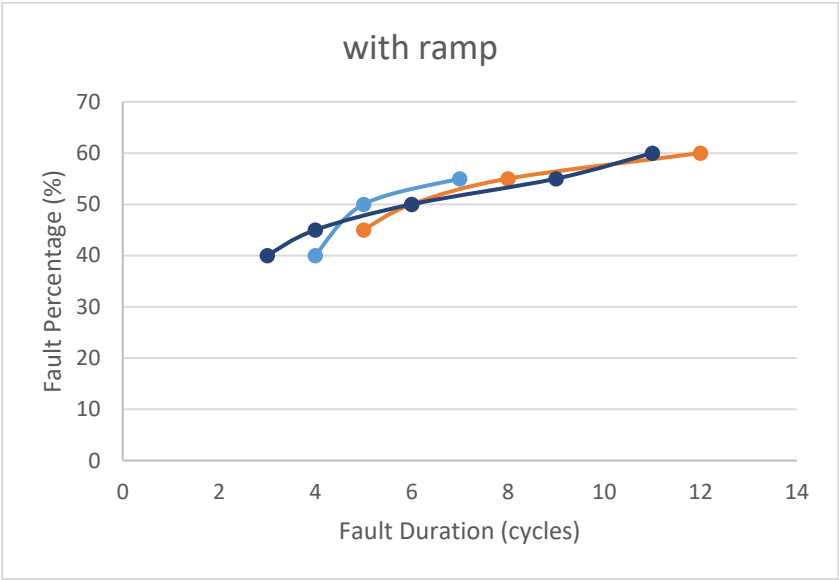


Fig 4.20 Stall analysis for reciprocating compressor with voltage ramp

As shown in Fig. 4.19 the stall behavior of the reciprocating compressor with non-ramp fault can be predicted by the model well. The prediction is off by one cycle only when voltage fault is 50% at zero-crossing. The ramp fault stall behavior is summarized in Fig. 4.20. The prediction is still good for zero-crossing. However, for the peak it is not as precise as that of the non-ramp fault. Additional study for the ramp fault can be performed to model the ramp fault.

The stall behavior of the motor with scroll compressor as load is shown in Table 4.5 to Table 4.10. Similarly, the case with voltage fault at peak with no ramp is used as the nominal case to tune the parameters. Also, for the voltage fault at zero crossing with no ramp case, the measure data stall at 1 cycle, which is captured by the simulation. And for the cases with ramp faults, the simulation result is able to match the measured data well.

Table. 4.5 Voltage Fault at Peak with no ramp (scroll compressor)

| Voltage Fault | Measured Stall Duration (cycles) | Simulation Stall Duration (cycles) |
|---|---|---|
| 30% | 4 | 4 |
| 35% | 5 | 5 |
| 40% | 6 | 6 |
| 45% | 7 | 7 |
| 48% | 9 | 9 |

| Table 4.6 Voltage Fault at zero crossing with no ramp (scroll compressor) | | |
|---|---|---|
| Voltage Fault | Measured Stall Duration (cycles) | Simulation Stall Duration (cycles) |
| 30% | N/A | N/A |
| 35% | N/A | N/A |
| 40% | N/A | N/A |
| 45% | N/A | 1 |
| 48% | 1 | 1 |

| Table 4.7 Voltage Fault at 45 degree with no ramp (scroll compressor) | | |
|---|---|---|
| Voltage Fault | Measured Stall Duration (cycles) | Simulation Stall Duration (cycles) |
| 30% | 1 | 2 |
| 35% | 1 | 2 |
| 40% | 3 | 3 |
| 45% | 5 | 4 |
| 48% | 6 | 6 |

| Table 4.8 Voltage Fault at Peak with ramp (scroll compressor) | | |
|---|---|---|
| Voltage Fault | Measured Stall Duration (cycles) | Simulation Stall Duration (cycles) |
| 30% | 2 | 2 |
| 35% | 3 | 3 |
| 40% | 4 | 4 |
| 45% | 5 | 6 |
| 48% | 8 | 8 |

| Table 4.9 Voltage Fault at zero crossing with ramp (scroll compressor) | | |
|---|---|---|
| Voltage Fault | Measured Stall Duration (cycles) | Simulation Stall Duration (cycles) |
| 30% | 3 | 2 |
| 35% | 3 | 3 |
| 40% | 5 | 4 |
| 45% | 6 | 6 |
| 48% | 8 | 8 |

| Table 4.10 Voltage Fault at 45 degree with ramp (scroll compressor) | | |
|---|---|---|
| Voltage Fault | Measured Stall Duration (cycles) | Simulation Stall Duration (cycles) |
| 30% | N/A | 2 |
| 35% | 3 | 3 |
| 40% | 4 | 4 |
| 45% | 5 | 6 |
| 48% | 8 | 8 |

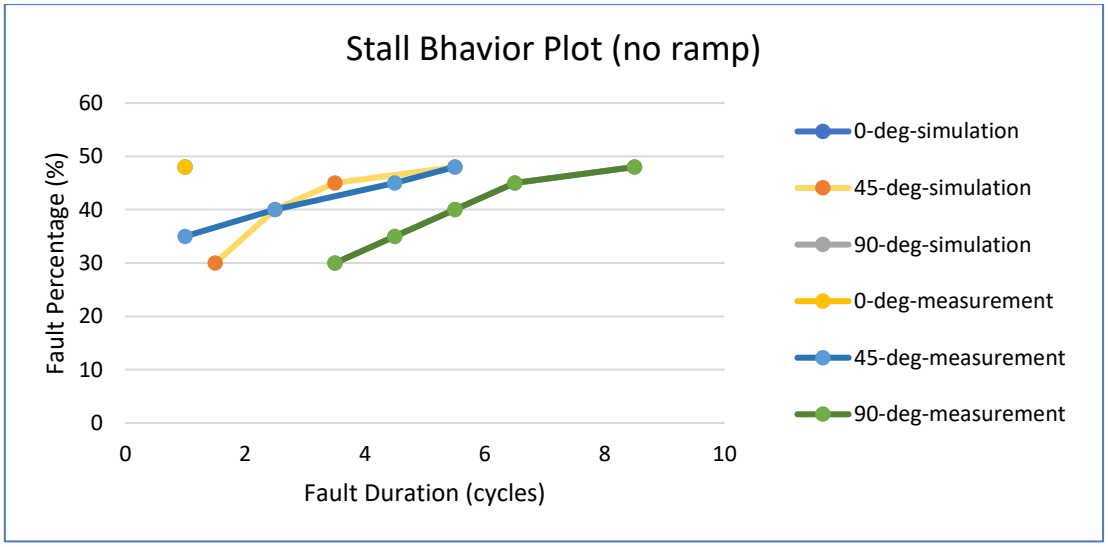


Fig 4.21 Stall analysis for scroll compressor with no voltage ramp

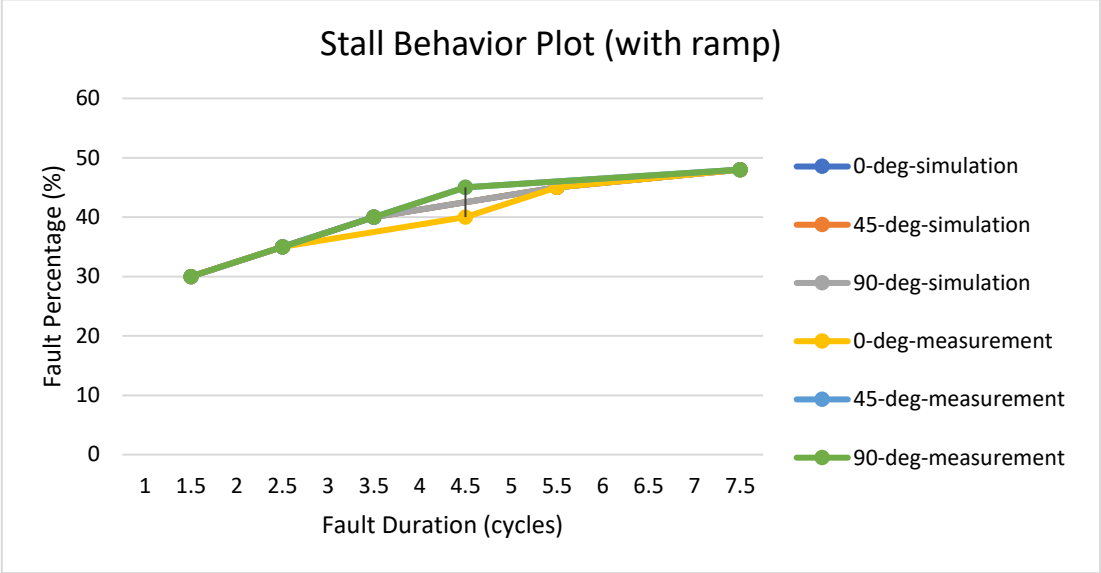


Fig 4.22 Stall analysis for scroll compressor with voltage ramp

As shown in Fig. 4.21 and Fig.22. The model for scroll compressor is able to match the peak fault with no ramp and it also matches the instantaneous stall for zero-crossing faults. The 45-degree fault and ramp fault are also predicted well.

# Chapter 5 *Conclusions and Recommended Future Work*

## 5.1 Conclusion

The goal of this project is to model the stall behavior of the two-phase induction motor for FIDVR analysis. The conclusions of the research are summarized here.

The two-phase induction machine is modeled using the machine equations with a point on wave model and a dynamic phasor model. The point on wave model is a more detailed method for the modeling. However, the dynamic phasor model is more useful for positive sequence simulation.

The load torque model for different compressors is modeled. The scroll compressor has a load torque nearly linearly proportional to the speed of the motor, while the reciprocating compressor has a larger torque variation related to the angular position.

The gas pressure is also modeled since the gas pressure is the major component of the load torque and inertia, which are the key factors that determine the stall behavior of the motor. Thus, the gas pressure model, where gas pressure is related to the speed of the motor is developed. The gas pressure model allows the simulation results to match the measurement in stall behavior at peak point fault.

The fault point would affect the stall behavior of the motor, and the point on wave model can capture that while dynamic phasor model cannot. So, the voltage phasor angle injection model is developed to compensate for the dynamic phasor model. The angle injection model helps to simulates the stall behavior at different fault point.

Parameters Estimation Model is developed to find the optimal parameters that match the steady state of simulation with measurement.

## 5.2 Future Work

***Develop the temperature model.***

The ambient temperature also has significant impact on FIDVR and it is not modeled here. More measurements about the temperature could be performed and the temperature model can be developed in the future.

***A more detailed load model can be developed from a mechanical engineer perspective.***

In this research, the load model is a simplified approximated model. The model can be expanded with detail modeling of the gas pressure and other mechanical variables in the system.

***Study the special behavior of the A/C.***

In this research, the model focuses on the motor and compressor structure. While the A/C unit has some abnormal behavior that the motor and compressor model cannot explain itself, such as the fast depletion of gas pressure and the current going to zero

after stalling. These may be caused by the load protection of the A/C and can be study and model.

***How does stalling related to FDVIR***

The reason for motor stalling is modeled in this research, but how it relates to FDVIR is not studied. This can be and needs to be studied in the future.

# *References*


[1] P.C. Krause, O. Wasynczuk, and S.D. Sudhoff, “Analysis Of Electric Machinery And Drive Systems,” second edition, IEEE press, 2002.

[2] B. Lesieutre, D. Kosterev and J. Undrill, "Phasor modeling approach for single phase A/C motors," *2008 IEEE Power and Energy Society General Meeting - Conversion and Delivery of Electrical Energy in the 21st Century*, Pittsburgh, PA, 2008, pp. 1-7.

[3] A. M. Stankovic, B. C. Lesieutre and T. Aydin, "Modeling and analysis of single-phase induction machines with dynamic phasors," in *IEEE Transactions on Power Systems*, vol. 14, no. 1, pp. 9-14, Feb 1999

[4] L. Creux, “Rotary Engine", US.P.801,182, 1905.

[5] K. Tojo, “Scroll Compressor With Means For End Plate Bias And Cooled Gas Return To Sealed Compressor Spaces", US 4216661.

[6] J. Tischer and R. Utter, "Scroll Machine Using Discharge Pressure For Axial Sealing", US 4522575.

[7] J. Caillat, R. Weatherston and J. Bush, "Scroll-Type Machine With Axially Compliant Mounting", US 4767293.

[8] H. Richardson, Jr., "Scroll Compressor With Orbiting Scroll Member Biased By Oil Pressure", US 4875838.

[9] S. Etemad, D. Yannascoli and M. Hatzikazakis, "Scroll Machine With Wraps Of Different Thicknesses", US 4834633.

[10] E. Morishita, M. Sugihara, T. Inaba and T. Nakamura, "Scroll Compressor Analytical Model", *International Compressor Engineering Conference*. Paper 495, 1984.

[11] H.P. Bloch and J.J. Hoefner, "Reciprocating Compressors, Operation and Maintenance." *Gulf Professional Publishing*, 1996.

[12] P R. G. Kurka, Karen L. G. Paulino and Jaime H. Izuka, "Dynamic Modeling of Reciprocating Compressors with Vertical Axis", *International Conference on Noise and Vibration Engineering (ISMA)/Conference of USD*, pp1573-1587, 2010.

[13] H. Seyrkammer, K. Schlacher and H. Westermayr, "Nonlinear control of a turbocharged diesel engine using singular perturbation methods," *2007 European Control Conference (ECC)*, Kos, 2007, pp. 1553-1560.

[14] Gavin, Henri P. "The Levenberg-Marquardt Method for Nonlinear Least Squares Curve-fitting Problems." people.duke.edu. 22 Mar. 2017. Web. 1 Apr. 2017.

[15] A. Björck. "Numerical methods for least squares problems", SIAM, Philadelphia, 1996.

[16] D.W. Marquardt. “An algorithm for least-squares estimation of nonlinear parameters,” *Journal of the Society for Industrial and Applied Mathematics*, 11(2):431-441, 1963.

[17] M.I.A. Lourakis. “A brief description of the Levenberg-Marquardt algorithm implemented by levmar”, *Technical Report, Institute of Computer Science*, Foundation for Research and Technology - Hellas, 2005.

[18] K. Madsen, N.B. Nielsen, and O. Tingleff. “Methods for nonlinear least squares problems.” *Technical Report. Informatics and Mathematical Modeling*, Technical University of Denmark, 2004.

[19] J. Pedra, “On the Determination of Induction Motor Parameters From Manufacturer Data for Electromagnetic Transient Programs,” *in IEEE Transactions on Power Systems*, vol. 23, no. 4, pp. 1709-1718, Nov. 2008.

[20] R. J. Bravo, R. Yinger and P. Arons, "Fault Induced Delayed Voltage Recovery (FIDVR) indicators," *2014 IEEE PES T&D Conference and Exposition*, Chicago, IL, USA, 2014, pp. 1-5.

[21] R. J. Bravo and D. P. Chassin, "Fault Induced Delayed Voltage Recovery (FIDVR) model validation," *2016 IEEE/PES Transmission and Distribution Conference and Exposition (T&D)*, Dallas, TX, 2016, pp. 1-4.